Cell

Article

Time-resolved single-cell transcriptomics defines immune trajectories in glioblastoma

Graphical abstract

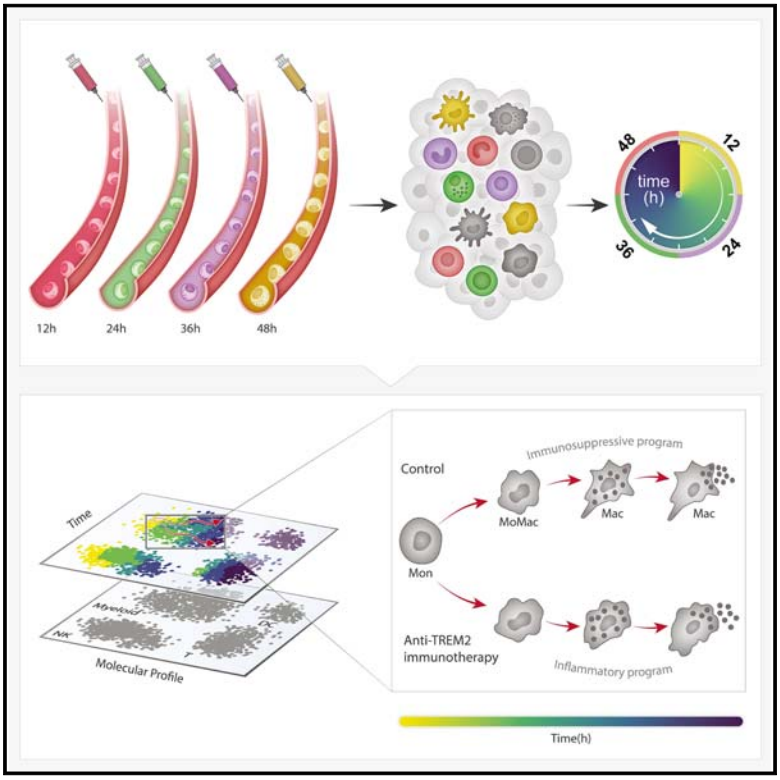

Authors

Daniel Kirschenbaum, Ken Xie, Florian Ingelfinger, ..., Tobias Weiss, Assaf Weiner, Ido Amit

Correspondence

ido.amit@weizmann.ac.il

In brief

A technology for *in vivo* recording of scRNA-seq with time (Zman-seq) revealing the temporal sequence of molecular changes in the tumor microenvironment that lead to immune dysfunction in glioblastoma.

Highlights

- Zman-seq a new technology for *in vivo* recording of scRNA-seq and time
- Temporally resolves cell-state transitions and molecular circuitry
- Reveals trajectories of immune dysfunction in glioblastoma
- Uncovers immune remodeling in response to experimental TREM2 immunotherapy

Kirschenbaum et al., 2024, Cell *187*, 149–165
January 4, 2024
https://doi.org/10.1016/j.cell.2023.11.032

CellPress

Cell

CellPress

Article

Time-resolved single-cell transcriptomics defines immune trajectories in glioblastoma

Daniel Kirschenbaum,[1,10] Ken Xie,[1,10] Florian Ingelfinger,[1,10] Yonatan Katzenelenbogen,[1,10] Kathleen Abadie,[1,10] Thomas Look,[2] Fadi Sheban,[1] Truong San Phan,[1] Baoguo Li,[1] Pascale Zwicky,[1] Ido Yofe,[1] Eyal David,[1] Kfir Mazuz,[1] Jinchao Hou,[3] Yun Chen,[3] Hila Shaim,[4] Mayra Shanley,[4] Soeren Becker,[5] Jiawen Qian,[6] Marco Colonna,[3] Florent Ginhoux,[6,7,8] Katayoun Rezvani,[4] Fabian J. Theis,[5] Nir Yosef,[1,8,9] Tobias Weiss,[2] Assaf Weiner,[1,11] and Ido Amit[1,11,12,*]

[1]Department of Systems Immunology, Weizmann Institute of Science, 7610001 Rehovot, Israel
[2]Department of Neurology, Clinical Neuroscience Center, University Hospital Zurich and University of Zurich, Zurich, Switzerland
[3]Department of Pathology and Immunology, Washington University School of Medicine, St. Louis, MO 63110, USA
[4]Department of Stem Cell Transplantation and Cellular Therapy, the University of Texas MD Anderson Cancer Center, Houston, TX 77030, USA
[5]Institute of Computational Biology, Helmholtz Zentrum München, German Research Center for Environmental Health, Neuherberg, Germany
[6]Shanghai Institute of Immunology, Department of Immunology and Microbiology, Shanghai Jiao Tong University School of Medicine, Shanghai 200025, China
[7]Singapore Immunology Network (SIgN), Agency for Science, Technology and Research, Singapore 138648, Singapore
[8]Department of Electrical Engineering and Computer Sciences, University of California, Berkeley, Berkeley, CA, USA
[9]Center for Computational Biology, University of California, Berkeley, Berkeley, CA, USA
[10]These authors contributed equally
[11]Senior author
[12]Lead contact
*Correspondence: ido.amit@weizmann.ac.il
https://doi.org/10.1016/j.cell.2023.11.032

SUMMARY

Deciphering the cell-state transitions underlying immune adaptation across time is fundamental for advancing biology. Empirical *in vivo* genomic technologies that capture cellular dynamics are currently lacking. We present Zman-seq, a single-cell technology recording transcriptomic dynamics across time by introducing time stamps into circulating immune cells, tracking them in tissues for days. Applying Zman-seq resolved cell-state and molecular trajectories of the dysfunctional immune microenvironment in glioblastoma. Within 24 hours of tumor infiltration, cytotoxic natural killer cells transitioned to a dysfunctional program regulated by TGFB1 signaling. Infiltrating monocytes differentiated into immunosuppressive macrophages, characterized by the upregulation of suppressive myeloid checkpoints *Trem2*, *Il18bp*, and *Arg1*, over 36 to 48 hours. Treatment with an antagonistic anti-TREM2 antibody reshaped the tumor microenvironment by redirecting the monocyte trajectory toward pro-inflammatory macrophages. Zman-seq is a broadly applicable technology, enabling empirical measurements of differentiation trajectories, which can enhance the development of more efficacious immunotherapies.

INTRODUCTION

"Wherever anything lives, there is, open somewhere, a register in which time is being inscribed."—Henri Bergson (Creative Evolution, 1911). All multicellular systems function through dynamic and coordinated action of cell circuits that change their activity in response to environmental signals. Single-cell RNA sequencing (scRNA-seq) has dramatically improved our ability to measure cell states at high resolution and scale. However, due to the destructive nature of the methodology, scRNA-seq can only capture static snapshots of gene expression at experimental endpoints, thus fundamentally omitting the temporal dimension. Despite this limitation, scRNA-seq profiling at multiple time points in dynamic processes has provided insight into transcriptional drivers of development and differentiation in myriad systems.[1–3] Computational approaches, such as pseudotime and RNA velocity estimations, infer a temporal dimension in scRNA-seq experiments either by ordering cells along a trajectory based on gene expression similarity or by estimating the time derivative of gene expression state by distinguishing spliced and unspliced mRNAs, respectively.[1,4–7] While these approaches are extremely useful, these algorithmic tools are sensitive to user-defined parameters and lack an empirically measured ground truth, making it difficult to test imputed

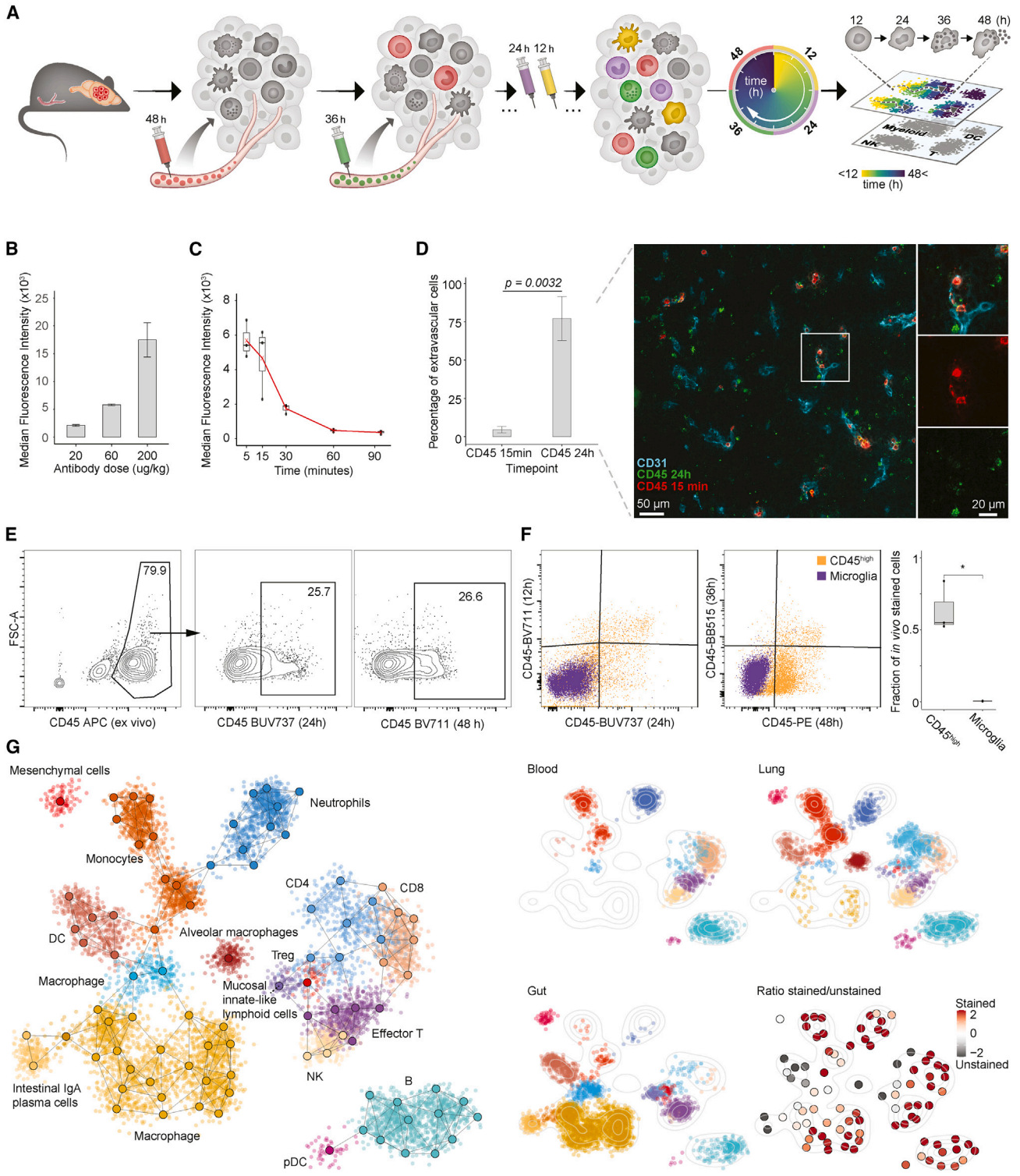

Figure 1. Zman-seq facilitates tracing of transcriptomic cell states *in vivo* across time

(A) Schematic illustration of the Zman-seq experimental and computational pipeline.

(B) Median fluorescence intensity bar chart of CD45⁺ PBMC after increasing concentrations of CD45-PE antibody intravenous injections, measured with flow cytometry. Error bars indicate mean and 90% CI (n = 3).

(legend continued on next page)

conclusions, particularly in complex *in vivo* settings where multiple trajectories may coexist.[8,9] Alternatively, combining scRNA-seq with metabolic labeling of new mRNA molecules offers a more direct measurement of gene expression changes over time and has provided insight into rapid cellular responses to stimuli such as viral entry, glucocorticoid receptor activation, and T cell signaling.[10] However, metabolic labeling is currently best suited for measuring processes that unfold over hours, and it is difficult to apply *in vivo* and to differentiation processes that span multiple days.

In solid tumors, immune cells that enter the tumor become subject to and complicit in supporting the immunosuppressive tumor microenvironment (TME), characterized by limited metabolic resources and immunosuppressive secreted factors.[11,12] Intratumoral T and natural killer (NK) cells transition from a functional cytotoxic state to a dysfunctional state characterized by upregulation of inhibitory receptors, loss of cytotoxicity, and loss of inflammatory cytokine secretion.[13,14] Myeloid cells, especially monocytes, are instructed by the TME to differentiate into tumor-associated macrophages (TAMs), producing ligands and checkpoints that further contribute to T and NK cell dysfunction, such as interleukin-10 (IL-10) and transforming growth factor β (TGF-β).[15] scRNA-seq analyses of millions of tumor-infiltrating immune cells across a wide range of mouse models and thousands of patient samples have comprehensively characterized the dysfunctional and immunosuppressive cell states that arise in cancer. However, despite these advances, the precise trajectories that newly infiltrating immune cells take to reach these dysfunctional states, the molecular circuits involved, and the timescales over which they unfold remain obscured. Resolving immune cell-state transitions in the TME in real time requires genomic methods that simultaneously collect both gene expression and time labels in single cells—relative to a relevant frame of reference.

We set out to understand how functional immune cells transition to dysfunctional states upon infiltrating the TME. We developed Zman-seq (זְמַן, Hebrew for "time", pronounced [zman]), an *in vivo* technology that adds temporal information to scRNA-seq data. Zman-seq provides empirical time measurements for tissue exposure of immune cells relative to fluorophore pulse labels applied in circulation. Using Zman-seq, we reconstructed the progression of immune cell states across time in the TME in a syngeneic orthotopic murine model for glioblastoma (GBM), a frequent, highly malignant and deadly brain tumor with an exceptionally immunosuppressive TME.[16] Zman-seq resolved the key immune trajectories in the tumor, including the progression of homing cytotoxic NK cells to states with low cytotoxic anti-tumor activity in ~24 h and monocytes to immunosuppressive TAMs. Further, it revealed time-dependent gene modules, transcription factor (TF) circuits orchestrating these trajectories, and key time-dependent receptor-ligand interaction events driving tumor immune evasion. We found the expression of *Trem2*, a key differentiation signal for TAMs,[17] to increase with time as monocytes progressed to TAMs. Blocking TREM2, using an antagonistic monoclonal antibody, redirected the monocyte differentiation trajectory toward pro-inflammatory macrophages, suggesting that myeloid reprogramming strategies may represent an attractive immunotherapy direction. In summary, Zman-seq experimentally introduces time stamps into immune cells and reveals a plethora of time-dependent transcriptomic, signaling and cell-cell interaction events. By introducing the temporal dimension into single-cell transcriptomic data, Zman-seq paves the way to dynamic models of multicellular systems *in vivo* with broad applicability. Zman-seq will be instrumental in resolving the dynamics of the TME to develop the next generation of immunotherapies.

RESULTS

Zman-seq resolves *in vivo* transcriptomic cell states across time

Cells respond to external stimuli by changing their functional state over time. To dissect how cells are reprogrammed *in vivo* upon exposure to a new environment, we developed Zman-seq, a technology combining fluorescent temporal tracking of cells with scRNA-seq (Figure 1A). Zman-seq is based on a physical barrier separating two biological compartments such that labeling (pulse) of cells only occurs in one compartment, allowing for cell tracking across compartments (chase). We took advantage of this pulse-chase principle and fluorescently labeled the circulating immune compartment with a temporal sequence of fluorophores in a syngeneic model for GBM (GL261). Leukocytes could be fluorescently labeled while in the vasculature but were shielded from consecutive rounds of labeling once they left the circulation and entered the tissue/tumor. Immune cells within the tumor were profiled using fluorescence-activated cell sorting

(C) Median fluorescence intensity boxplots of CD45$^+$ PBMC after mixing with blood from mice injected with CD45-PE antibody for increasing durations (see Figure S1B). Staining intensity of PBMC decreases with longer incubation times in the donor mouse. Each dot represents a sample and the box extends to the 25th and 75th percentile with the median in bold line (n = 3).

(D) Histology of GBM brain tumors (GL261) from mice intravenously injected with CD45 antibody 24 h (BB515, green) and 15 min (PE, red) before tumor extraction. Bar chart showing the percentage of extravascular (defined based on endothelia stained with CD31, blue) cells harboring the 24-h or 15-min staining. Error bars indicate mean and 90% CI (n = 3), and the p value was calculated using a two-sided Wilcoxon test.

(E) Flow cytometry density plots of CD45$^+$ cells from GL261 tumor after intravenous fluorescent CD45 antibody injections 24, 36, 48, and 60 h (see also Figure S1D) before tumor extraction.

(F) Flow cytometry dot plots and boxplots of CD45$^+$ cells from GL261 tumor showing the *in vivo* CD45 antibody time labeling (CD45-PE/BB515/BUV737/BV711) of microglia and CD45^{high} infiltrating leukocytes. Infiltrating leukocytes harbor significantly more temporal labeling, compared with microglia (p = 0.02434, n = 3). Each dot represents a sample and the box extends to the 25th and 75th percentile with the median in bold line.

(G) Metacell graph projection of CD45$^+$ cells from blood, colon, and lung pooled (left) and separated by organ (right), consisting of 91 MCs representing 8,976 pooled single cells sorted from 3 mice submitted to Zman-seq (12-, 24-, 36-, and 48-h time stamps), and a heatmap of time-stamped/non-stained CD45$^+$ cell ratio.

See also Figures S1 and S2.

(FACS), and fluorescent stamps on individual cells were captured using index sorting to infer the time of tumor infiltration. This enabled us to define the time each immune cell spent in the tumor—termed tumor exposure time. Combining tumor exposure time measurements with single-cell transcriptomic profiling, Zman-seq generates temporal maps of the TME.

In order to establish an *in vivo* labeling protocol, we titrated the staining of peripheral blood mononuclear cells (PBMCs) by intravascular injections of fluorescent anti-CD45 antibodies. Concentrations ranging from 20 to 200 μg/kg body weight (bw) stained the entirety of PBMCs (99.8% ± 0.26%, n = 9), with the mean fluorescent intensity increasing with antibody dose (Figures 1B and S1A). To ensure that Zman-seq faithfully measures tumor exposure time between a labeling event in the circulation and harvest in the tumor, it was critical to validate that our fluorescent antibody injections specifically label circulating immune cells and not tumor-resident immune cells. Reasoning that any non-specific labeling of tumor-resident immune cells would require extravasation of antibodies into the tumor and would therefore be highly influenced by plasma antibody concentrations, we first measured the kinetics of unbound antibody levels in the circulation (Figures 1C and S1B). We found that the amount of unbound antibody available for staining decays rapidly, dropping below detection level 60 min after injection, likely a consequence of high blood CD45 antigen levels and in agreement with published data.[18] Building on this, we then performed histological analysis on GL261 tumors from mice injected with fluorescent anti-CD45 antibodies 15 min (when the unbound plasma-antibody concentration was still sufficiently high) and 24 h before harvest. This analysis demonstrated significantly more extravascular localization of the 24-h labeled cells, compared with the 15-min labeled cells: while 84.8% (±5.9% confidence interval, n = 3) of the 15-min signal was intravascular, after 24 h 80% (±13.6%) of the signal shifted to the extravascular compartment (Figures 1D and S1C). Importantly, there was no non-specific labeling of tumor-resident immune cells at the 15-min time point. We next analyzed the effective time window of Zman-seq labeling by quantifying fluorescently labeled circulating $CD45^+$ cells that extravasate to the tumor over a range of labeling time points spanning biologically relevant tumor-immune exposure times. To this end, we injected anti-CD45 antibodies every 12 h between 60 and 24 h prior to GL261 tumor harvest, using a set of distinct fluorophores for every time point. We detected fluorescently labeled leukocytes in the tumor from all injection time points, demonstrating the applicability of Zman-seq to processes unfolding over multiple days in the tumor (Figures 1E and S1D). To evaluate the rate of false-positive Zman-seq labeling, we analyzed $CD45^+$ cell labeling in the brain after 12-, 24-, 36-, and 48-h time stamps. We found that microglia, resident brain macrophages that express CD45 and are entirely of yolk sac origin, were not labeled with any of the anti-CD45 time stamp injections, highlighting the selectivity of the method to unambiguously label circulating leukocytes (Figures 1F and S1E). To further estimate the time window for which labeled cells can be tracked using Zman-seq, we labeled PBMCs from B6.SJL mice carrying the CD45.1 allele with anti-CD45-PE antibody *ex vivo* and transferred the cells into CD45.2 recipient mice. Notably, we observed that anti-CD45-PE-labeled CD45.1 leukocytes could be reliably detected in the blood across immune cell subsets for 96 h and longer (Figure S1F). Altogether, the rapid decay of unbound anti-CD45 antibody in circulation, combined with the accumulation of sparsely distributed labeled immune cells in the tumor and no off-target labeling of microglia, is consistent with the desired properties of specific and stable high-resolution (~30 min) stamping of circulating immune cells.

Specific detection of labels from each time point enabled grouping of leukocytes into tumor exposure time bins based on their fluorescent profiles recorded during single-cell FACS index sorting. Tumor exposure time was determined based on the last antibody a cell was exposed to in the circulation (Figure S2A; STAR Methods). For example, a cell was considered in the 36-h tumor exposure time bin if it was only labeled with the 36-h fluorophore but also if it was additionally labeled with the 48- and/or 60-h fluorophores—meaning that the cell was in circulation and exposed to antibody injections between 60 and 36 h before it entered the tumor and was shielded from the 24-h injection. To assess whether our empirical time measurement methodology could be generalized to peripheral organs beyond the central nervous system, we benchmarked Zman-seq in the physiological steady state of colon and lung tissues by injecting 12-, 24-, 36-, and 48-h anti-CD45 time stamps. The profiled leukocytes showed remarkable organ-specific cell-state adaptation, compared with circulating leukocytes, highlighting the potential of Zman-seq to investigate time-resolved immune cell adaptation (Figure 1G). We detected robust time stamp signals across all immune cell states except for embryonically derived alveolar macrophages, tissue-resident intestinal innate-like lymphoid cells, and intestinal IgA plasma cells—highlighting the exclusion of time stamps from long-term tissue-resident cells of the colon and the lung and thus the broad applicability of Zman-seq to profile cellular dynamics of diverse tissues (Figures 1G, S2B, and S2C). Collectively, we demonstrate that time-stamping, using sequential *in vivo* injections of fluorescently labeled antibodies, facilitates a robust methodology to trace cellular and molecular kinetics of leukocytes across different organs in healthy and diseased states.

Temporal dynamics of the TME in GBM

GBM is the most frequent and aggressive lethal primary brain malignancy in adults, with a gold standard radio-chemotherapy protocol that has not been significantly improved for two decades, thus remaining a major unmet need.[19] The lack of successful immunotherapy approaches in GBM highlights a need to better understand and curtail immunosuppressive differentiation trajectories in the TME. For this purpose, we used Zman-seq (labeling 12-, 24-, and 36-h time stamps) and measured scRNA profiles of 10,583 high-quality leukocytes sorted from the TME of the murine syngeneic GL261 glioma model, simultaneously with tumor exposure time stamps. We grouped these cells by their transcriptomes into 139 metacells (MCs) containing 55–170 cells/metacells.[20] We identified a large myeloid compartment consisting of monocytes (*Plac8*$^+$, *Chil3*$^+$), TAMs (*Trem2*$^+$, *Arg1*$^+$), and dendritic cells (DCs) (*H2-Oa*$^+$). Lymphocytes in the tumor comprised $CD4^+$ T helper cells, $CD8^+$ cytotoxic T cells, T regulatory cells, and NK cells. NK cells could be further subsetted into chemotactic (*S1pr5*$^+$), cytotoxic/effector (*Prf1*$^+$, *Gzma*$^+$,

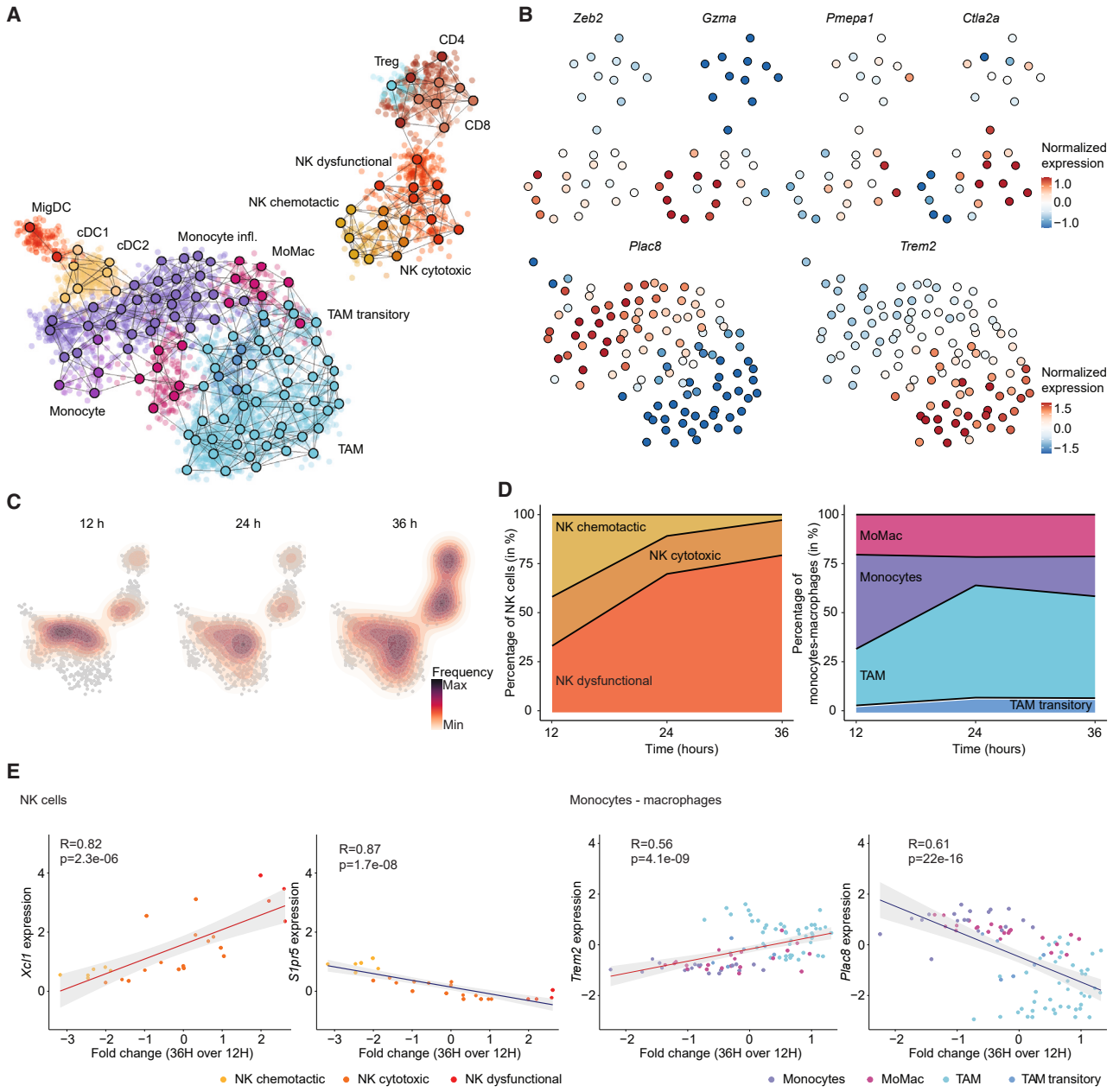

Figure 2. Zman-seq resolves temporal dynamics of the TME in glioblastoma

(A) Two-dimensional graph projection of 139 metacells representing 10,584 single cells sorted from CD45$^+$ gating from GL261 GBM tumors.

(B) Marker gene projections of $\log_2$ normalized footprint expression on lymphocytes (top) and myeloid cells (bottom), respectively.

(C) Density enrichment of cells from each labeled time bin downsampled to 250 cells per time bin from CD45$^+$ gated cells.

(D) Stacked percentage area plot that shows the relative percentage of cells at each time bin (12, 24, and 36 h, respectively). The left plot shows the distribution of NK subtypes across time bins, and the right plot shows the distribution of cells from the mononuclear phagocyte populations.

(E) Correlation plots of $\log_2$ normalized footprint marker expression against time enrichment in NK cells (left panel showing *XCL1* and *S1pr5* expression) and mononuclear phagocyte populations (right panel showing *Trem2* and *Plac8* expression). The x axis represents the $\log_2$ enrichment of 36-h time bin over 12-h time bin where positive values represent enrichment in 36-h time bin and vice versa. The Spearman's correlation rho and p value are shown, and the fitted regression line shows a 95% confidence interval.

See also Figure S2.

and *Gzmb*$^+$), and dysfunctional (*Itga1*$^+$, *Xcl1*$^+$, *Eomes*$^-$, and *Pmepa1*$^+$), with the latter resembling signatures of NK cells exposed to TGF-β[21–24] (Figures 2A, 2B, S2D, and S2E; Table S1). Leukocytes assigned to 12-, 24-, or 36-h tumor exposure time bins clustered distinctly (Figures 2C and S2F), suggesting an association between tumor exposure time and immune

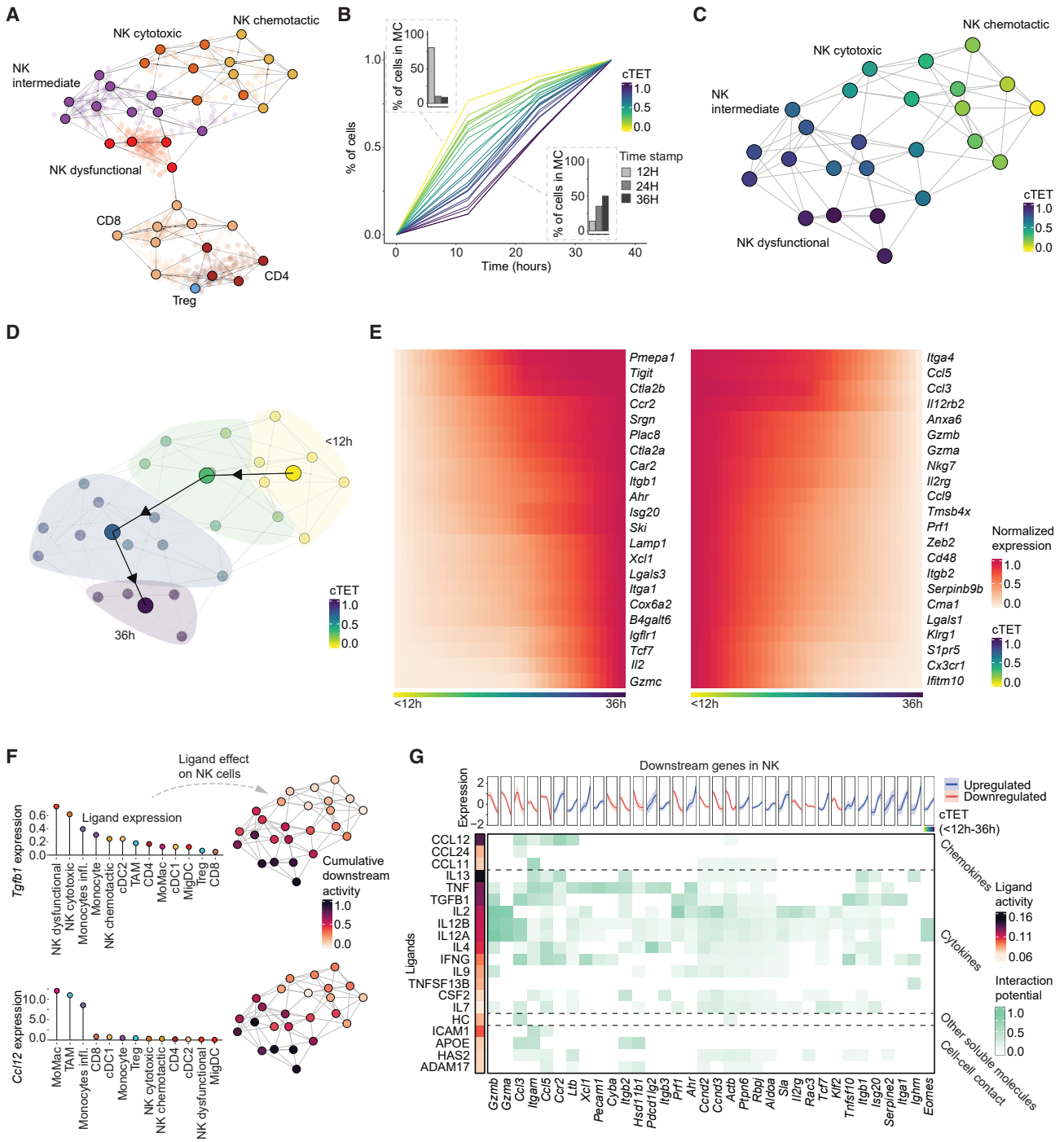

Figure 3. Zman-seq reveals temporal NK cell trajectories in the tumor

(A) Two-dimensional graph projection of reclustered lymphocytes consisting of 37 metacells representing 2,431 single cells, including NK cells, CD8 T cells, and CD4 T cells.

(B) Cumulative sum distribution plot of each time bin (12, 24, and 36 h) in each metacell. Each line represents a metacell, and the color denotes the normalized area under the curve that we define as cTET. The dotted boxes show the distribution of normalized frequency of each time bin within the earliest cTET metacell (top left) and the longest cTET metacell (bottom right).

(C) Projection of normalized cTET values onto the NK subpopulations as annotated in (A).

(D) Base trajectory inference of the time development along the cell types from the earliest cTET chemotactic NK to the latest cTET dysfunctional NK. The shaded color represents the cell-type clusters, and the four trajectory points correspond to the cluster average cTET. The trajectory arrows are drawn based on the ordering of average cTET (STAR Methods).

(legend continued on next page)

cell functional states. Analysis of the distribution of cell types in the 12-, 24-, and 36-h tumor exposure time bins corresponded with specific cell states. To better resolve cellular states, we increased the MC resolution and reclustered the myeloid and lymphoid cell compartments separately. Indeed, chemotactic (*S1pr5*$^+$) and cytotoxic (*Prf1*$^+$, *Gzma*$^+$, and *Gzmb*$^+$) NK cells showed high enrichment in early (12-h) time points, whereas dysfunctional NK cells (*Itga1*$^+$, *Ctla2a*$^+$, *Gzmc*$^+$, and *Prf1*/*Gzma*/*Gzmb*-low) were enriched in later (24- to 36-h) time points—suggesting that Zman-seq captured biologically plausible and relevant information of the NK response to tumor signals[21,22] (Figures 2D and S2G). For instance, Ducimetiere and colleagues described a set of NK clusters: mature/effector (*Gzma*$^+$, *Zeb2*$^+$, *Prf1*$^+$, and *Klrg1*$^+$ cNK_5), immature (*Ctla2a*$^+$ and *Ccr2*$^+$ cNK_4), and TGF-β-imprinted (*Gzmc*$^+$, *Pmepa1*$^+$, *Xcl1*$^+$, and *Ctla2a*$^+$ cNK_6) NK cells found only in immunologically cold tumors, which aligned well with the clusters we defined with distinct temporal kinetics (Figure S2H). The myeloid compartment showed a similar association of differentiation and time, with monocytes (*Ear2*$^+$, *Ace*$^+$, *Chil3*$^+$, and *Plac8*$^+$) harboring early (12-h) time stamps and TAMS (*C1qa*$^+$, *Trem2*$^+$, and *Arg1*$^+$) harboring late time stamps, consistent with the expected transition of circulating monocytes to TAMs in the tumor (Figures 2C and 2D).[24] These cell-state changes upon exposure to the TME were associated with extensive molecular dynamics. For instance, in NK cells the expression of the homing receptor *S1pr5* decreased with time, whereas *Xcl1* expression, a chemoattractant for DCs, increased. Similarly, in the myeloid compartment, the expression of *Plac8*, highly expressed in monocytes,[24,25] decreased with tumor exposure time, whereas the expression of the myeloid checkpoint *Trem2* increased (Figure 2E). In summary, we demonstrate that Zman-seq is capable of resolving fine-grained temporal gene expression trends during assembly of the TME, thereby providing a technology to resolve immune escape mechanisms evoked by the tumor.

Molecular trajectories of NK cell dysfunction in GBM

A limitation of most single-cell transcriptome atlases is the inability to empirically define cellular trajectories over time. To overcome this limitation in our GBM model, we annotated immune cell states at high resolution and leveraged our temporal labeling to track transcriptional trajectories between states (Figures 3A and S3A; Table S1). To translate single-cell time stamps to a time axis over which to observe differentiation trajectories, we developed a robust statistical method to assign continuous tumor exposure time (cTET) values on the MC level (Figure S3B; STAR Methods). For each MC, we calculated a cumulative distribution function (CDF) based on the frequency of cells in 12-, 24-, and 36-h bins (Figures 3B, S3B, and S3C). For each MC CDF, the area under the curve (AUC) represents the cTET. Overlaying the AUC profile on the MC map elucidated the gradual shift of cell states across time (Figure 3C). We then used the average cTET for each annotated cell cluster (Figure 3A) to define the trajectory underlying these observed cell-state transitions (Figure 3D). Next, we temporally ordered MCs by cTET and identified the most significant genes correlating with time (Figure 3E; Table S1). This approach revealed multiple gene expression changes unfolding at different rates in response to tumor exposure. Genes that were upregulated immediately upon tumor exposure included the TGF-β response genes *Pmepa1* and *Srgn*, NK immaturity markers *Ccr2* and *Tcf7*,[22] as well as the inhibitory checkpoint receptor *Tigit*.[26] Upregulation of TGF-β-driven *Car2* and *Ctla2a*, previously shown to hamper NK anti-tumor activity, closely followed, along with *Xcl1* and *Itga1*.[22] *Gzmc* expression, also shown to be TGF-β driven, increased rapidly during the final stage of the trajectory—suggesting that major biomarkers of NK exposure to GBM TME are TGF-β-associated signaling modules and are indicators of the duration of TGF-β exposure. Genes that were immediately downregulated upon tumor exposure include homing receptors (*S1pr5* and *Cx3cr1*) and NK effector and maturity markers (*Klrg1* and *Cma1*).[27–29] Expression of inflammatory cytokines and cytotoxic molecules (*Ccl3*, *Gzmb*, *Gzma*, and *Prf1*) decreased more gradually[30] (Figure 3E).

To identify the drivers of these transcriptional dynamics, we next estimated the TF activities of each MC, based on the average gene expression signature of the gene targets of each TF, using the dorothea database[31] (Figure S3D; STAR Methods). This analysis revealed anti-correlated activity over time of SMAD3 and SMAD4, critical downstream mediators of TGF-β signaling. SMAD3 relays TGF-β signaling, leading to reduced cytotoxicity in NK cells,[30] whereas SMAD4 counteracts this effect.[32] Consistently, Zman-seq showed that SMAD4 was initially active for a sustained period, counteracting TGF-β signaling, followed by a rapid drop at the end of the temporal trajectory that coincided with a spike in SMAD3 activity orchestrating TGF-β signaling and leading to the emergence of the TGF-β-imprinted dysfunctional NK cell state. Additionally, the activity of TFs involved in NK differentiation, maturation, and interferon-γ (IFN-γ) signaling decreased along the temporal trajectory at distinct rates: decrease in GATA3 activity was gradual, whereas FOSL2 and GATA2 were faster.[33–35]

A core focus in immuno-oncology is to understand interactions in the tumor-immune environment leading to ineffective

(E) Heatmaps of significantly upregulated (left) or downregulated (right) genes across cTET in NK cells. Each row is normalized and smoothed according to the cTET of each metacell and shows the transitioning of genes from chemotactic NK to dysfunctional NK as ordered by cTET.
(F) Lollipop plot (left) and MC map (right) displaying the predicted time-dependent interaction between NK cells and the TME. Lollipop plots show the normalized gene expression of the two ligands *Tgfb1* and *CCL12* across cell types (potential senders). MC maps are colored by the scaled weighted cumulative target gene expression of TGF-β1- and CCL12-regulated target genes in NK cells.
(G) Heatmap (middle) showing the interaction potential for the 20 most prioritized ligands and their respective target genes in NK cells that correlate with time. Ligands have been prioritized by their capability to explain gene expression changes across time in NK cells. Heatmap (left) indicates the predicted activity for each ligand. Ligands have been manually grouped into biologically relevant subtypes. Line plots (top) display scaled gene expression of target genes in NK cells across time (red = downregulated, blue = upregulated, shaded area = 90% confidence intervals).
cTET, continuous tumor exposure time.
See also Figure S3.

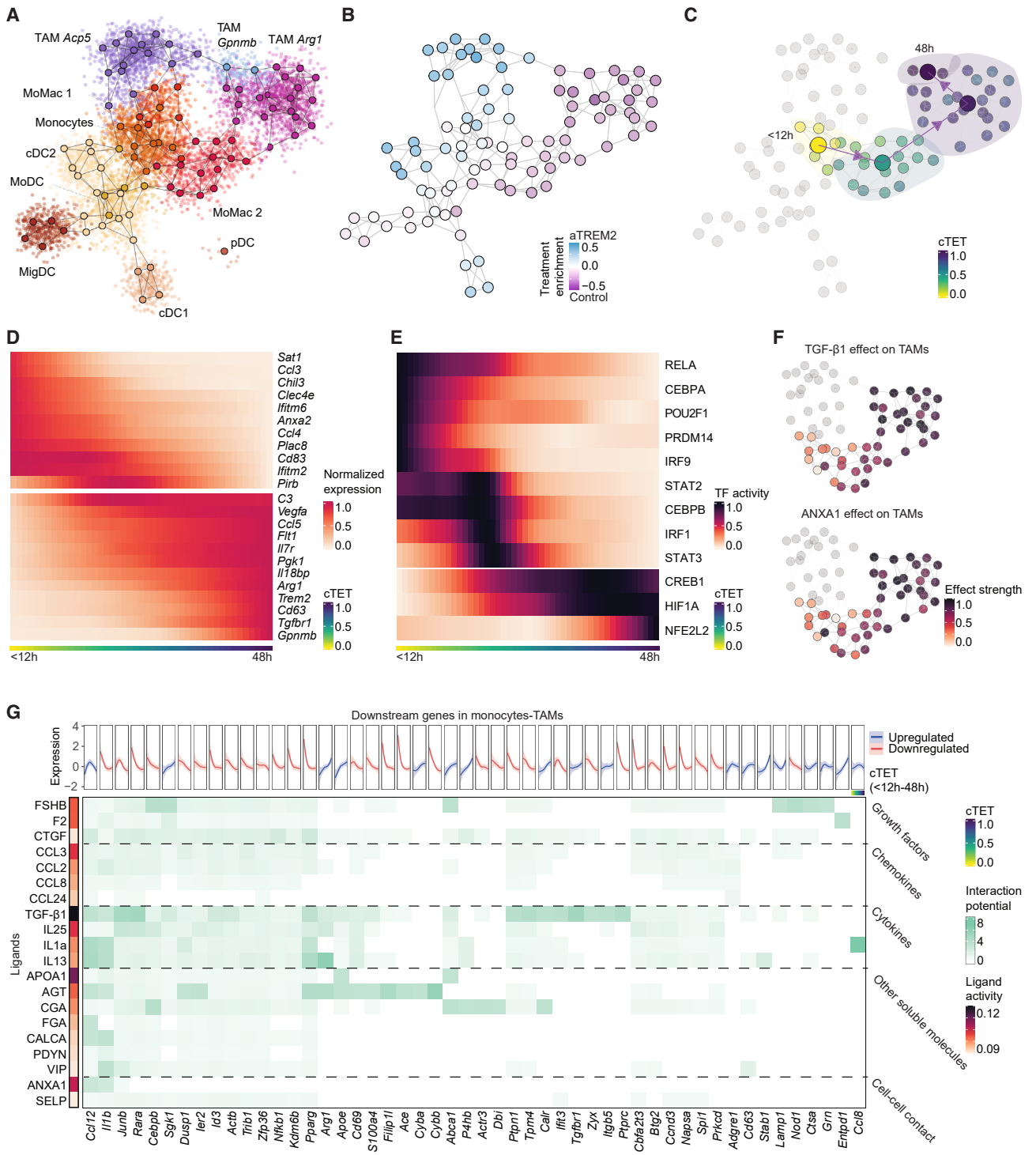

Figure 4. Zman-seq reveals monocytes-to-TAM differentiation in GBM

(A) Metacell graph projection of myeloid cells consisting of 94 MCs representing 7,421 single cells sorted from 3 IgG control mice and 3 aTREM2-treated mice on CD45$^+$ gating.

(B) Projection of treatment enrichment by the number of cells of each condition within a metacell. The enrichment is log scaled where positive values indicate enrichment upon aTREM2 treatment, and negative values represent control enrichment.

(C) Trajectory of the monocyte-to-TAM differentiation in the control axis based on cTET values. The shaded color represents the cell-type clusters, and each of the four points in the trajectory corresponds to the cluster average cTET.

(legend continued on next page)

anti-tumor immunity. Zman-seq provides a critical analytical tool to identify ligands that reprogram immune cells into a tumor-tolerant state upon TME exposure (Figure S3E). To infer putative upstream ligands that may drive the observed immune-escape gene programs in NK cells, we prioritized ligands based on their ability to explain the temporal gene expression changes detected using Zman-seq. Consistent with the TGF-β-responsive gene expression module and TF activity dynamics we observed, this analysis revealed TGF-β1 as a major ligand driving the NK dysfunctional trajectory in the TME (Figures 3F, 3G, S3F, and S3G). Additional predicted ligands driving NK dynamics included the macrophage-derived chemokine CCL12 and cell-cell contact ligands ICAM1 and APOE (Figures 3F, 3G, S3F, and S3G). However, TGF-β1 explained almost exclusively the temporal transition of *Itga1*^{low} to *Itga1*^{high} NK cells with concomitant reduction in cytotoxic activity (*Gzmb* and *Prf1*; Figure 3F). Late dysfunctional NK cells had high *Tgfb1* expression, although contribution by resident non-immune cells of the microenvironment, such as tumor cells, stromal cells, or microglia, also appears likely[36] (Figure 3F). We next used functional assays on primary human patient samples to ask whether the data showing that TGF-β signaling in the GBM TME inhibits NK cell cytotoxicity translate to human pathology in GMB patients. By co-culturing human glioma stem cells with primary human NK cells *in vitro*, we evaluated degranulation (CD107a), tumor necrosis factor alpha (TNF-α), and IFN-γ expression in response to TGF-β blockade (Figure S3H).[37] Consistent with the dynamics we observed using Zman-seq in the mouse model, we found a strong negative association between TGF-β signaling and the production of cytotoxic molecules and inflammatory cytokines in human NK cells (Figure S3H). Altogether, we demonstrate a principled analytical framework for Zman-seq data and how it can resolve the complex trajectory of NK cells and the signaling and TF circuitry of the TME, leading to a gradual decline in NK cytotoxic activity in contribution to tumor immune escape.

Temporal molecular trajectories of the mononuclear phagocyte system in the TME

TAMs are a major component of the immunosuppressive TME and are key to tumor persistence.[38] TAMs in GBM originate from infiltrating circulating monocytes and local microglia.[39] Characterizing the molecular trajectories of the mononuclear phagocyte system in the TME is crucial for better understanding the signals and pathways associated with immune dysfunction in GBM and solid tumors in general. We found a strong correlation between tumor exposure time and *Trem2* expression (Figures 2B and 2E), an immunosuppressive signaling hub for macrophages.[17] Previous studies have shown that genetic ablation of *Trem2* or blocking TREM2 with monoclonal antibodies modifies TAMs and evokes anti-tumor immunity.[40–42] These studies raise the question of whether blocking TREM2 affects mature *Trem2*$^{+}$ TAM function or acts earlier in the differentiation of monocytes into TAMs. To address this question and to define monocyte-to-TAM differentiation in the presence and absence of TREM2 signaling, we treated six mice with an antagonistic antibody targeting TREM2 (aTREM2) and six mice with a control antibody at days 2 and 7 post tumor implantation, similar to Molgora and colleagues (Figure S4A).[40] Then, 11 days after tumor implantation, leukocytes were time-stamped 12, 24, 36, and 48 h before tissue harvesting. Control mice recapitulated the TME composition observed previously, including activated and dysfunctional NK states, infiltrating monocytes, DCs, and TAMs (Figures 2, 4A, and S4B–S4D; Table S2). The myeloid compartment of mice treated with the aTREM2 antibody contained macrophage cell states highly separated from those in the control antibody-treated mice (Figure 4B). In mice treated with the control antibody, Zman-seq revealed a well-defined temporal trajectory of monocyte to TAMs: infiltrating *Chil3*^{high}, *Plac8*^{high} monocytes harbored the earliest time stamps and gradually differentiated to *Arg1*^{high}, *Gpnmb*^{high} regulatory macrophage populations, described in the context of immunosuppressive myeloid cells in cancer (Figures 4C, S4E, and S4F).[41] The expression of genes promoting immunosuppression in the TME showed distinct temporal patterns along this trajectory (Figure 4D; Table S2). The first changes were related to differentiation from the monocyte state by decreasing the expression of *Plac8* and *Chil3*. In parallel, *Sat1* and *Ccl3*, genes involved in inflammatory processes,[43,44] rapidly decayed in monocytes. This was followed by a rapid increase in the expression of macrophage programs and pro-tumorigenic factors such as *C3*, as well as the pro-angiogenic factor *Vegfa* and its receptor *Flt1*.[45–47] Simultaneously, *Pirb* (LILRB3), an inhibitory receptor that binds to major histocompatibility complex class 1 (MHC class I) instructing immunosuppressive TAM differentiation,[48] was transiently upregulated at the monocyte-macrophage

(D) Heatmaps of significantly upregulated (top) or downregulated (bottom) genes across cTET in control monocyte-to-TAM differentiation. Each row is normalized and smoothed according to the cTET of each metacell and shows the dynamics of gene expression along the monocyte-to-TAM^{Gpnmb} transition as ordered by cTET.

(E) Heatmaps of significantly upregulated (top) or downregulated (bottom) transcription factor (TF) activities across cTET in the control monocyte-to-TAM differentiation. Each row is normalized and smoothed according to the cTET of each metacell and shows the transitioning of TF activity from monocyte to TAM^{Gpnmb} as ordered by cTET.

(F) Metacell map displaying the predicted time-dependent interaction between mononuclear phagocytes (monocytes, MoMacs, and TAMs) and the TME. Metacell maps are colored by the scaled weighted cumulative target gene expression, termed "effect strength", of TGF-β1- and ANXA1-regulated target genes in mononuclear phagocytes.

(G) Heatmap (middle) showing the interaction potential for the 20 most prioritized ligands and their respective target genes in mononuclear phagocytes that correlate with time. Ligands have been prioritized by their ability to explain gene expression changes across time in mononuclear phagocytes. Heatmap (left) indicates the predicted activity for each ligand. Ligands were manually grouped into biologically relevant subtypes. Line plots (top) display scaled gene expression of target genes in mononuclear phagocytes across time (red = downregulated, blue = upregulated, shaded area = 90% confidence intervals).

cTET, continuous tumor exposure time; MoMac, monocyte-derived macrophages; TAM, tumor-associated macrophage.

See also Figures S4 and S5.

junction. This was followed by robust activation of tumor macrophages programs with upregulation of immunosuppressive pathways *Arg1*, *Cd274 (PDL1)*, and *Il18bp*,[24,49] followed by *Trem2* and *Gpnmb*, a hallmark for suppressive Mregs, peaking in the terminal sections of the temporal trajectory.[41]

Analysis of the TF circuits regulating this myeloid trajectory revealed distinct temporal patterns, including the downregulation of pro-inflammatory and upregulation of immunosuppressive TF circuits (Figure 4E). Downregulation of nuclear factor κB (NF-κB)-associated RELA activity, together with POU2F1 involved in inflammatory macrophage activation, was among the first TF responses upon monocyte tumor exposure.[50,51] This was followed by loss of STAT2 and IRF9 activity, key nodes in antiviral pathways.[52,53] The final step of reprogramming toward TAM included upregulation of immunosuppressive STAT3 activity, followed by monotonical upregulation of HIF1A and CREB1 activity, involved in hypoxic suppressive TAM function and suppressive macrophage polarization, respectively.[54–56] The terminal portion of our analyzed trajectory was characterized by high NFE2L2 activity, involved in suppressing inflammatory cytokine secretion in macrophages.[57]

We next applied these temporal data to analyze the upstream ligands that may drive the differentiation process from infiltrating monocytes to TAMs, potentially representing attractive targets for immunotherapy (Figures S3E, S5A, and S5B). The ligands that best explained the trajectory from monocytes to TAMs included pro-tumorigenic TGF-β1 and ANXA1 and pro-inflammatory APOA1, whereas chemokines (e.g., CCL2, CCL3, and CCL8) contributed less[58–60] (Figures 4F, 4G, and S5C). The cumulative expression of target genes regulated by TGF-β1 and ANXA1 was relatively low in monocytes and increased along the temporal trajectory until its peak in *Arg1*^{high} and *Gpnmb*^{high} TAMs (Figure 4F). The number of time-dependent genes affected by a given ligand was highly variable; for instance, TGF-β1 or CCL3 and CCL2 contributed to a broad set of target genes, whereas ANXA1 only affected the upregulation of monocyte recruitment via CCL12 and the downregulation of inflammatory factors *Il1b* and *Junb*.[61] *Arg1*, a metabolic immunosuppressive hallmark gene of TAM differentiation, was influenced by only a few pro-tumorigenic ligands: TGF-β1, IL-13, and AGT[62,63] (Figure 4G). To assess whether TGF- β1 could indeed orchestrate the observed cell trajectory from circulating monocytes to pro-tumorigenic TAMs, we differentiated murine bone-marrow-derived myeloid cells in the presence or absence of TGF-β1 and confirmed the emergence of regulatory macrophage cell states expressing *Il18bp* and *Gpnmb in vitro* (Figure S5D).

To evaluate to what extent the Zman-seq-resolved trajectory of the mononuclear phagocyte compartment in GL261-bearing mice reflected human pathology in GBM patients, we next analyzed publicly available transcriptomic data of human GBM patients. We tested how genes controlling the myeloid trajectory across time in murine GBM relate to myeloid states found in human GBM patients (Figure S5E).[24] Murine genes defining early cell states of the trajectory (Figure 4D, upper panel) aligned with monocyte and inflammatory TAM states in humans, whereas late genes (Figure 4D, lower panel) overlapped with regulatory lipid TAMs and phagocytic TAMs—suggesting robust translation of the murine temporal results to human data. Overall, Zman-seq enabled *in vivo* characterization of the molecular trajectory of monocyte differentiation to regulatory macrophages, which are a major driver of the immune dysfunction in the GBM TME. Our analysis lays the foundation for improved understanding of myeloid reprogramming in the tumor and for identifying effective molecules that antagonize regulatory macrophage differentiation in the TME.

Blocking TREM2 signaling redirects the monocyte-to-macrophage trajectory in the TME

Next, we assessed how TREM2 antagonistic immunotherapy influenced the differentiation of the mononuclear phagocyte system in GBM. Three of the six mice treated with aTREM2 antibody showed marked differences in their respective TME, compared with control mice (indicating an immunological response), whereas three mice showed more subtle perturbation. As expected, *Trem2*-expressing myeloid cells, such as TAMs and monocyte-derived macrophages, responded most to the TREM2 antagonistic therapy, indicating that the efficacy of the therapy may be attributed to direct effects on *Trem2*-expressing cells (Figures S5F and S5G). We compared myeloid cells of mice treated with aTREM2 with myeloid cells of mice treated with the control antibody, and we used Zman-seq to investigate the immune dynamics of the two treatment groups (Figure 4B). aTREM2 treatment resulted in a distinct TAM population, compared with the control group, characterized by downregulation of immunosuppressive genes such as *Arg1*, *Pirb* (LILRB3), *Il18bp*, *Vegfa*, and *Cd274* (PDL1) and upregulation of pro-inflammatory genes (*Ccl3*, *Ccl4*, *Cd81*, and *Cd83*), in line with previous reports.[40,41,64,65] These two distinct TAM populations developed through a striking bifurcation of monocyte-to-TAM trajectory (Figures 5A and 5B; Table S3). We utilized this dataset as a ground truth to perform detailed analytical benchmarking and compared the performance of computational approaches with our empirical time measurement methodology (summarized in STAR Methods; Figure S6). In short, trajectories predicted by commonly used pseudotime and RNA velocity algorithms showed variable results, strongly depending on the selection of genes. These comparisons highlight the limitations of current computational approaches to resolve cellular trajectories and demonstrate the synergy of combining analytical and empirical time measurements in single-cell transcriptomic studies.

To better understand the mechanism of action of anti-TREM2 immunotherapy, we next investigated the trajectory bifurcation elicited by the treatment. The roots of both the control and aTREM2 trajectories were similar, consisting of infiltrating monocytes that did not express *Trem2* (Figure S4D). In both groups, initial state transitions entailed the downregulation of monocyte transcripts (*Chil3* and *Plac8*) (Figure 5C; Table S2). We observed immediate and late transcriptomic changes distinguishing the control and aTREM2 trajectories. Early changes upon TREM2-inhibition included the rapid upregulation of pro-inflammatory factors *Ccl4* and *Cd81* and inhibition of early upregulation of immunosuppressive factors seen in the control group (e.g., *Pirb* and *Vegfa*).[45–47] In monocyte-derived macrophages, aTREM2 elicited a transient upregulation of an IFN-induced gene module including *Ifit2* and *Ifit3*.[66] This was followed by

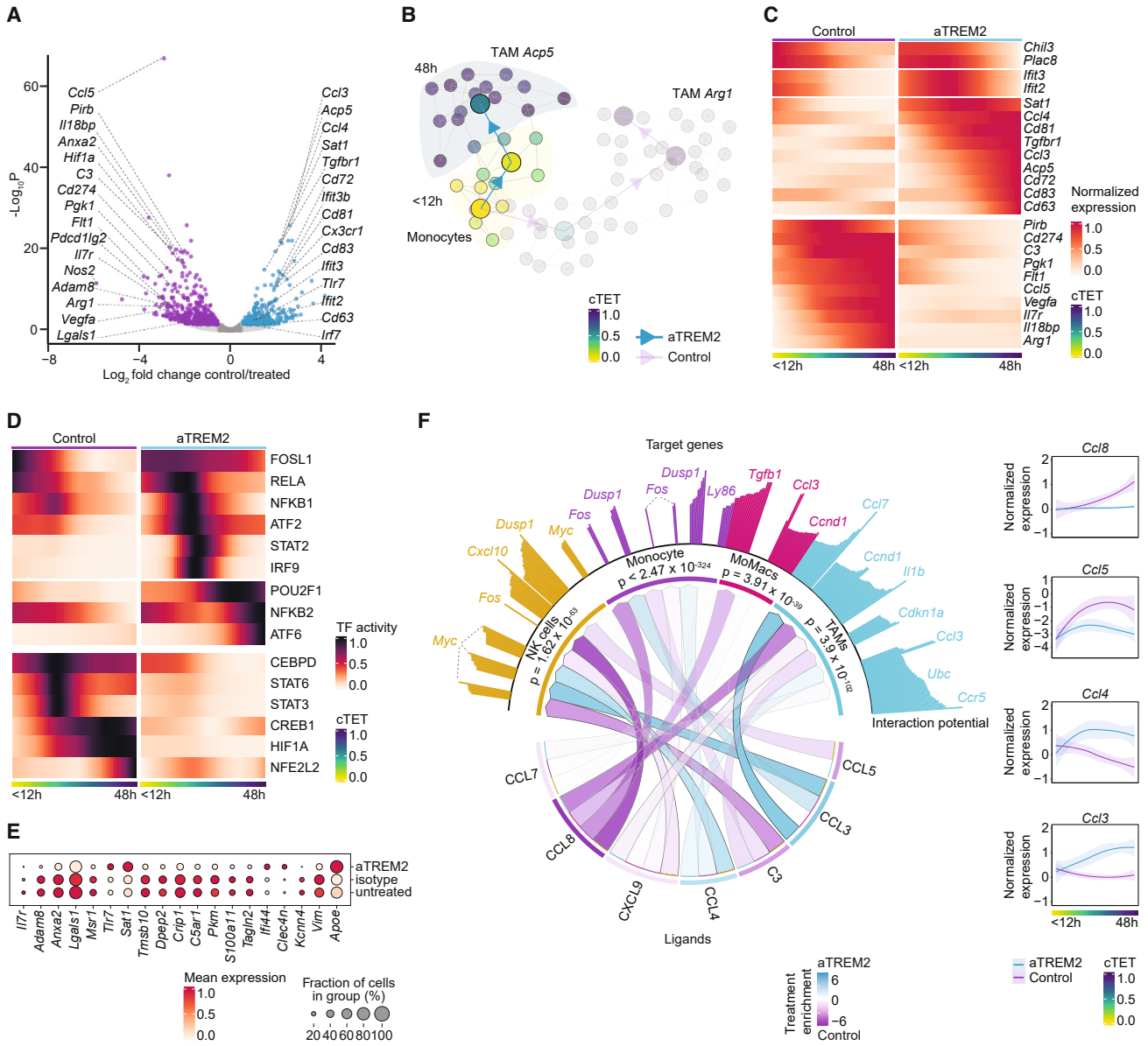

Figure 5. TREM2 antagonistic antibody reprograms the TME by disrupting monocyte-to-TAM transition

(A) Volcano plot depicting the differential genes between the *Arg1* TAMs of the IgG treatment against the *Acp5* TAMs of the aTREM2 treatment. The significant genes ($p < 0.001$ and $\log_2$ fold change > 0.5) were colored purple if they were enriched in IgG treatment and blue if enriched in aTREM2 treatment.

(B) Metacell graph projection of monocytes and TAMs from both IgG and aTREM2 axis, denoting the trajectory of the aTREM2-treated monocyte-to-TAM differentiation based on cTET. The shaded color represents the cell clusters, and each of the three points in the trajectory corresponds to the cluster average cTET.

(C) Heatmaps of significant genes along cTET in the aTREM2-treated monocyte-to-TAM differentiation. Each row is normalized and smoothed according to the cTET of each metacell and shows the transitioning of genes from monocyte to *Acp5* TAMs as ordered by cTET.

(D) Heatmaps of significant TF activity along cTET in the aTREM2-treated monocyte-to-TAM differentiation. Each row is normalized and smoothed according to the cTET of each metacell and shows the transitioning of TF activity from monocyte to *Acp5* TAMs as ordered by cTET.

(E) Dot plot displaying the normalized gene expression of *in vitro* differentiated BMDMs cultured with GL261 cell culture supernatant in the presence of TREM2-blocking antibody or isotype or PBS control. Dot size indicates percentage of cells expressing the respective gene, and color indicates scaled mean gene expression per group.

(F) Circos plot (left) indicating the interaction between chemokine ligands produced by *Trem2*-expressing cells (senders) and receiver cell types (as presented in Figures S9A–S9D). Color indicates the $\log_2$ fold change enrichment for each ligand upon TREM2 inhibition. Outer semi-circle displays the interaction potential between each ligand and the top 20 affected target genes per cell type. Line plots (right) showing scaled expression of chemokine ligands produced by monocyte-derived phagocytes (monocytes, MoMacs, and TAMs) across time for aTREM2-treated mice (blue) and mice receiving isotype control (purple). Expression has been smoothed using a polynomial regression model, and mean and 95% confidence intervals (shaded area) are shown.

BMDMs, bone-marrow-derived macrophages.

See also Figures S5 and S7.

TAMs upregulating additional pro-inflammatory markers (*Ccl3*, *Acp5*, and *Cd72*),[64,65,67] and downregulating immunosuppressive genes (*Arg1*, *Il18bp*, and *Il7r*).

TF activity analysis identified regulators of the pro-inflammatory trajectory induced by TREM2 inhibition (Figure 5D). Early on, FOSL1, part of the AP-1 TF complex enhancing inflammation by inhibiting *Arg1* transcription,[68] showed high activity in monocytes and maintained this throughout the trajectory of macrophages treated with aTREM2 antibody. TFs showing high transient activity in monocyte states included components of the NF-κB complex, such as RELA (p65) and NFKB1 (p50), forming a heterodimer and promoting pro-inflammatory transcriptional programs.[69] ATF2, indicated in inflammatory macrophages,[70] showed a similar early transient activity as NFKB1. Slightly later, in the monocyte-macrophage junction, pro-inflammatory STAT2 and IRF9 involved in IFN signaling showed a transient activity peak. In parallel, aTREM2 treatment downregulated the immunosuppressive activities of STAT3 and STAT6.[52,71] In the final TAM program, aTREM2 treatment induced pro-inflammatory NFKB2 activity (p52)[69] and inhibited the upregulation of immunosuppressive HIF1A and NFE2L2 activity.[54,57]

Differential gene expression analysis of TAMs during TREM2 inhibition revealed differentially abundant transcripts involved in metabolic functions, such as *Sat1*, *Arg1*, *and Hif1a*[72] (Figures 5A, 5C, and S5G). Similar changes in metabolic profile have previously been associated with the conversion of regulatory T cells to highly inflammatory T helper 17 cells.[73] It therefore appears plausible that an analog metabolic mechanism coexists during the conversion of monocytes to immunosuppressive TAMs and that this metabolic pathway is remodeled following TREM2 blockade. To assess whether the observed effects in TAMs were directly mediated by the aTREM2 antibody, we performed *in vitro* differentiation of bone-marrow-derived macrophages using varying doses of GBM-conditioned medium in the presence or absence of the aTREM2 antibody. Supplementing cell culture medium with varying doses of GL261 supernatant elicited a dose-dependent effect on the state of bone-marrow-derived macrophages, mimicking the *in vivo* TME (Figures S7A–S7C). Using these *in vitro* GBM TME conditions, we recapitulated several of the *in vivo* effects of TREM2 blockade in primary murine macrophages (Figures 5E and S7B). Moreover, we observed increased *Sat1* expression in bone-marrow-derived myeloid cells treated with aTREM2 antibody, indicating that the metabolic changes may be a direct consequence of TREM2 blockade (Figures 5E and S7B).

To obtain mechanistic insights into the environmental context in which aTREM2 treatment redirects TAM differentiation toward an inflammatory state, we investigated the potential downstream crosstalk of *Trem2*-expressing cells following aTREM2 treatment. We investigated ligand-receptor pairs that could explain the observed changes in target gene expression elicited by aTREM2 treatment in TAMs. Strikingly, a small set of ligands was predicted to explain a large portion of the downstream effects of TREM2 inhibition in TAMs ($p = 3.9 \times 10^{-102}$). These ligands were mostly restricted to the chemokines CCL3, CCL4, CCL5, CCL7, CCL8, and CXCL9 and complement factor C3 (Figures 5F and S7D–S7G). In addition to their predicted role, the same chemokines ranked among the most differentially expressed genes in TAMs following aTREM2 treatment (*C3*, *Ccl3*, *Ccl4*, *Ccl5*, *Ccl7*, *Ccl8*, and *Cxcl9*) and demonstrated temporal expression kinetics, providing further evidence that this set of chemokines may be crucial for the myeloid remodeling and even for clinical outcomes (CCL5, CCL7; $p = 0.016$ and $p = 0.029$, respectively) (Figures 5C, 5F, S7G, and S7H). Chemokine circuits have been reported to play a fundamental role in the establishment and modulation of the TME.[74] Thus, we next assessed whether the set of differentially abundant chemokines, which explained the majority of downstream signaling upon TREM2 inhibition in TAMs, may also affect neighboring leukocytes in a paracrine fashion. Interestingly, these chemokines and complement factor C3 showed widespread effects in modulating gene expression in receiver cells. The identified set of ligands explained a large fraction of the observed gene expression changes upon TREM2 inhibition in NK cells, monocytes, and monocyte-derived macrophages, providing a rationale for how modulating TAM differentiation may affect the organization of the TME (Figure 5F).

In summary, applying Zman-seq in a therapeutic context identified the capacity of TREM2 inhibition to reprogram the monocyte-to-regulatory macrophage trajectory and temporally resolved molecular circuits downstream of TREM2 that facilitate the transition of circulating monocytes to suppressive TAM.

DISCUSSION

Single-cell technologies opened a new chapter in biology by large-scale phenotyping of cells as the minimal unit of life. Analyzing millions of cells has provided seminal insights into cell states across diverse tissues and pathologies. Here, we addressed the fundamental question of how competent immune cells become an accomplice of the tumor, using Zman-seq, an *in vivo* scRNA-seq technology that empirically resolves immune cell-state transitions across time.

We applied Zman-seq to a murine syngeneic GBM model, aiming to resolve cell-state trajectories in infiltrating leukocytes. This analysis revealed rapid transition of NK cells from a cytotoxic to a dysfunctional state within 24 h. While transitioning through this trajectory, NK cells upregulated gene programs associated with TGF-β imprinting, in line with previously described tumor-associated NK cell studies.[22] Temporal ligand-receptor interaction analysis highlighted a set of ligands, including TGF-β1 and CCL12, as major factors dampening NK cell activity in the tumor. The advantage of empirically determined temporal dynamics via Zman-seq over conventional static sequencing approaches was exemplified by revealing a potential temporal TF circuit of coordinated SMAD3 and SMAD4 activities downstream of TGF-β, immediately preceding the emergence of the TGF-β-imprinted terminal NK state.[30,32] In the myeloid compartment, Zman-seq uncovered state transitions from early infiltrating monocytes to tumor-associated regulatory macrophages (Mreg) within 36–48 h.[41] Along this trajectory, monocytes transitioned through monocyte-derived macrophage and TAM states by upregulating immunosuppressive modules and downregulating pro-inflammatory modules. Upstream TF activities also showed increasing pro-tumor and decreasing anti-tumor activities across time, driven by signals such as TGF-β1 and ANXA1. Zman-seq also

highlighted immunosuppressive genes and TFs that showed distinct transient activity over time (e.g., LILRB3 and STAT3).[48] These examples showcase tightly coordinated gene and TF activities as components of the dynamic regulation of immunosuppression in the TME, only detectable with the unique temporal resolution that Zman-seq provides. This conceptual advance can be readily applied to develop the next generation of immunotherapeutic agents in a data-driven fashion by hijacking tumor escape modules. For instance, Zman-seq revealed that chemokines such as CCL5, produced by mature TAMs, may recruit circulating leukocytes such as monocytes and T cells into the TME, whereas the presence of TGF-β in the TME dramatically interfered with their anti-tumor effector function. Modulating both immune cell infiltration and effector functions of leukocytes may be promising strategies to combat difficult-to-treat tumors, and indeed, therapeutic application of molecules interfering with TGF-β and CCL5 signaling are currently being explored.[75,76] Zman-seq identifies gene modules that can be targeted to specifically interfere with critical checkpoints in immune cell differentiation, such as the monocyte to TAM transition.

Finally, we tested whether Zman-seq can uncover the mechanism of action of myeloid checkpoints and thereby help prioritize their application as monotherapy and in combination in pre-clinical trials. Inhibition of TREM2, a known signaling hub for immunosuppressive TAMs,[17] with an antagonistic antibody resulted in extensive direct effects in macrophages and secondary effects in other interacting cells, such as NK cells. Zman-seq showed that cells with the earliest time stamps comprised monocyte states that were shared across aTREM2-treated and control mice. However, after this early state, macrophages of aTREM2-treated mice followed a completely distinct TAM differentiation trajectory. In contrast to *Arg1*^{high} TAMs in control-treated mice, aTREM2 treatment resulted in *Acp5*^{high} and Cd72^{high} inflammatory TAMs. In progression to this state over time, macrophages increased pro-inflammatory signaling, decreased or reversed suppressive signaling, and in parallel exhibited significant metabolic changes. Temporally resolved ligand-receptor analysis revealed chemokines such as CCL3 and CCL4 as important signaling hubs mediating TME reprogramming in the context of TREM2 blockade. CCL3 is pro-inflammatory, recruiting T and NK cells but also recruiting TAMs.[77] Its cognate receptor CCR5 on TAMs promotes immunosuppression correlating with worse clinical outcomes—targeted in clinical trials.[78,79] TREM2 immunotherapy greatly increased *Ccl3* expression while decreasing its cognate receptor *Ccr5* on TAMs—suggesting that blocking TREM2 enhanced and channeled CCL3 signaling to support inflammation (Figure S7G).

The main goal of science, according to John von Neumann[80], is to generate models. In biology, the modeled systems are dynamic, that is, the components of the system change as a function of time. Thus, describing an endless number of single cells in minute detail will not result in useful scientific models, unless these observations are related to each other temporally. Along these lines, a recent study revealed causal links between genetic variants and the single-cell expression quantitative trait loci across the course of exogenous T cell activation. A large fraction of these genotype-to-phenotype links would have been omitted when analyzing time-agnostic static endpoints.[81] Similarly, a temporally resolved CRISPR-activation screen of single cells identified TFs regulating zygotic genome activation.[82] While the incorporation of the time component in these studies was crucial to understand how individual genes orchestrate cellular processes like activation or differentiation, they fail to capture the underlying complexity of intact multicellular organisms. With Zman-seq, an empirical tool to infer gene causalities *in vivo*, we usher in the next era of *in vivo* perturbation studies. Adding a temporal dimension to large-scale chemical drug screens in zebrafish models for inflammatory disorders[83] or genomic CRISPR screens in the context of tumor immunology[84] will provide a much-needed causal understanding of the influence of genes and the environment in biological systems. Time-stamping combined with lineage tracing approaches will provide valuable insights by integrating temporal dynamics with cell phylogeny estimates. The combination of Zman-seq with spatial transcriptomic methods will shed light on the temporal sequence of cell-cell interactions and their influence on cell state in tissue, leading to a quasi cinemagraphic window into biology. We show the utility of Zman-seq in a tumor model; however, it is also well suited to study models of infection, autoimmunity, and differentiation beyond immunology.

Overall, our work highlights that introducing a temporal dimension into otherwise static single-cell genomic experiments provides a conceptual advance with the unique opportunity to infer causality during cellular transitions. The application of Zman-seq to tumor immunology clarified the progression of immune dysfunction in the GBM TME and its rewiring under therapeutic intervention. Empirically resolving cell-state transitions across time is the only way toward dynamic models of complex cellular systems approaching reality—improving our understanding of physiology and diseases.

Limitations of the study

Zman-seq is an empirical *in vivo* single-cell technology providing a ground truth of state transitions of cells across time and thus can uncover fundamental insights into the biology of cell adaptions. Yet, Zman-seq in its current version has limitations that could be addressed in future studies. For example, the number of fluorescent time stamps is currently limited by the spectral overlap of available dyes. However, advances in fluorescent dyes and full spectrum analyzers virtually extend this to a total number of more than 40 detectable fluorophores.[85] In future studies, fluorophores could be replaced by oligonucleotide barcodes, thereby increasing the number of possible time stamps and ensuring compatibility with commercial droplet-based single-cell transcriptomics pipelines. Further, fluorescent signals fade with time after multiple days,[18] and in addition, cells might shed and recycle the CD45 epitope,[86] leading to loss of labeling and lower signal to noise for measurements of tissue exposure times longer than ~7 days.

STAR★METHODS

Detailed methods are provided in the online version of this paper and include the following:

- KEY RESOURCES TABLE

SUPPLEMENTAL INFORMATION

Supplemental information can be found online at https://doi.org/10.1016/j.cell.2023.11.032.

ACKNOWLEDGMENTS

We thank T. Bigdary and G. Brodsky from the Scientific Illustration unit of the Weizmann Institute for artwork. I.A. is an Eden and Steven Romick Professorial Chair, supported by the HHMI international scholar award. This work is funded by the European Union ERC advanced grant (no. 101055341-TROJAN-Cell), the Deutsche Forschungsgemeinschaft (DFG, German Research Foundation) – NeuroMac Project-ID 259373024 – TRR 167, the Israel Science Foundation (ISF) grant no. 1944/22, and by the Helen and Martin Kimmel Award for Innovative Investigation. The ISF Israel Precision Medicine Program (IPMP) 607/20. The MBZUAI-WIS Joint Program for Artificial Intelligence Research. The Dwek Institute for Cancer Therapy Research, the Moross Integrated Cancer Center, and the Swiss Society Institute for Cancer Prevention Research. D.K. is a recipient of the postdoctoral fellowship of the Swiss Friends of the Weizmann Institute of Science and of the Azrieli Foundation. K.X. and F.I. were funded by the Koshland award. F.I. is recipient of an EMBO postdoctoral fellowship. Y.K. is a recipient of the Azrieli Graduate Fellowship. K.A. was funded by a Fulbright Scholarship.

Sequencing data are available in NCBI GEO.

AUTHOR CONTRIBUTIONS

D.K. developed experimental protocol; conceptualized, designed, performed, and analyzed experiments and interpreted results; and wrote the manuscript. K.X. and F.I. designed and analyzed experiments, developed computational methods, performed bioinformatic analyses, and wrote the manuscript. Y.K. and F.S. designed, performed, and analyzed experiments. K.A. designed, performed, and analyzed experiments and wrote the manuscript. T.L. and T.W. contributed to the development of the experimental protocols and performed experiments. T.S.P., H.S., M.S., K.R., B.L., F.J.T., J.Q., and P.Z. performed experiments. I.Y. contributed to the development of the experimental protocols. E.D. and S.B. performed bioinformatic analyses. K.M. performed experiments. J.H., Y.C., and M.C. developed Fc-mutated aTREM2 antibody and control antibody. N.Y. and F.J.T. supervised bioinformatic analyses. A.W. conceptualized, designed, and analyzed experiments; developed computational methods; performed bioinformatic analyses; and wrote the manuscript. I.A. developed experimental protocols, directed the project, conceptualized and designed experiments, interpreted results, and wrote the manuscript.

DECLARATION OF INTERESTS

A.W. and I.A. are inventors of a patent related to TREM2 antibodies. I.A. is a member of the *Cell* Advisory Board. A patent application has been filed related to this work.

Received: May 2, 2023
Revised: September 15, 2023
Accepted: November 27, 2023
Published: December 21, 2023

REFERENCES

1. Ding, J., Sharon, N., and Bar-Joseph, Z. (2022). Temporal modelling using single-cell transcriptomics. Nat. Rev. Genet. *23*, 355–368.
2. Griffiths, J.A., Scialdone, A., and Marioni, J.C. (2018). Using single-cell genomics to understand developmental processes and cell fate decisions. Mol. Syst. Biol. *14*, e8046.
3. Kanton, S., Boyle, M.J., He, Z., Santel, M., Weigert, A., Sanchís-Calleja, F., Guijarro, P., Sidow, L., Fleck, J.S., Han, D., et al. (2019). Organoid single-cell genomic atlas uncovers human-specific features of brain development. Nature *574*, 418–422.
4. La Manno, G., Soldatov, R., Zeisel, A., Braun, E., Hochgerner, H., Petukhov, V., Lidschreiber, K., Kastriti, M.E., Lönnerberg, P., Furlan, A., et al. (2018). RNA velocity of single cells. Nature *560*, 494–498.
5. Trapnell, C., Cacchiarelli, D., Grimsby, J., Pokharel, P., Li, S., Morse, M., Lennon, N.J., Livak, K.J., Mikkelsen, T.S., and Rinn, J.L. (2014). The dynamics and regulators of cell fate decisions are revealed by pseudotemporal ordering of single cells. Nat. Biotechnol. *32*, 381–386.
6. Lange, M., Bergen, V., Klein, M., Setty, M., Reuter, B., Bakhti, M., Lickert, H., Ansari, M., Schniering, J., Schiller, H.B., et al. (2022). CellRank for directed single-cell fate mapping. Nat. Methods *19*, 159–170.
7. Bendall, S.C., Davis, K.L., Amir el, A.D., Tadmor, M.D., Simonds, E.F., Chen, T.J., Shenfeld, D.K., Nolan, G.P., and Pe'er, D. (2014). Single-cell trajectory detection uncovers progression and regulatory coordination in human B cell development. Cell *157*, 714–725.
8. Gorin, G., Fang, M., Chari, T., and Pachter, L. (2022). RNA velocity unraveled. PLoS Comput. Biol. *18*, e1010492.

9. Zheng, S.C., Stein-O'Brien, G., Boukas, L., Goff, L.A., and Hansen, K.D. (2022). Pumping the brakes on RNA velocity – understanding and interpreting RNA velocity estimates. bioRxiv. https://www.biorxiv.org/content/10.1101/2022.06.19.494717v1.

10. Erhard, F., Saliba, A.E., Lusser, A., Toussaint, C., Hennig, T., Prusty, B.K., Kirschenbaum, D., Abadie, K., Miska, E.A., Friedel, C.C., et al. (2022). Time-resolved single-cell RNA-seq using metabolic RNA labelling. Nat. Rev. Methods Primers *2*, 77.

11. Binnewies, M., Roberts, E.W., Kersten, K., Chan, V., Fearon, D.F., Merad, M., Coussens, L.M., Gabrilovich, D.I., Ostrand-Rosenberg, S., Hedrick, C.C., et al. (2018). Understanding the tumor immune microenvironment (TIME) for effective therapy. Nat. Med. *24*, 541–550.

12. Labani-Motlagh, A., Ashja-Mahdavi, M., and Loskog, A. (2020). The tumor microenvironment: a milieu hindering and obstructing antitumor immune responses. Front. Immunol. *11*, 940.

13. McLane, L.M., Abdel-Hakeem, M.S., and Wherry, E.J. (2019). CD8 T cell exhaustion during chronic viral infection and cancer. Annu. Rev. Immunol. *37*, 457–495.

14. Huntington, N.D., Cursons, J., and Rautela, J. (2020). The cancer-natural killer cell immunity cycle. Nat. Rev. Cancer *20*, 437–454.

15. Mantovani, A., Marchesi, F., Malesci, A., Laghi, L., and Allavena, P. (2017). Tumour-associated macrophages as treatment targets in oncology. Nat. Rev. Clin. Oncol. *14*, 399–416.

16. Medikonda, R., Dunn, G., Rahman, M., Fecci, P., and Lim, M. (2021). A review of glioblastoma immunotherapy. J. Neurooncol. *151*, 41–53.

17. Deczkowska, A., Weiner, A., and Amit, I. (2020). The physiology, pathology, and potential therapeutic applications of the TREM2 signaling pathway. Cell *181*, 1207–1217.

18. Potter, E.L., Gideon, H.P., Tkachev, V., Fabozzi, G., Chassiakos, A., Petrovas, C., Darrah, P.A., Lin, P.L., Foulds, K.E., Kean, L.S., et al. (2021). Measurement of leukocyte trafficking kinetics in macaques by serial intravascular staining. Sci. Transl. Med. *13*.

19. Stupp, R., Mason, W.P., van den Bent, M.J., Weller, M., Fisher, B., Taphoorn, M.J., Belanger, K., Brandes, A.A., Marosi, C., Bogdahn, U., et al. (2005). Radiotherapy plus concomitant and adjuvant temozolomide for glioblastoma. N. Engl. J. Med. *352*, 987–996.

20. Baran, Y., Bercovich, A., Sebe-Pedros, A., Lubling, Y., Giladi, A., Chomsky, E., Meir, Z., Hoichman, M., Lifshitz, A., and Tanay, A. (2019). MetaCell: analysis of single-cell RNA-seq data using K-nn graph partitions. Genome Biol. *20*, 206.

21. Gao, Y., Souza-Fonseca-Guimaraes, F., Bald, T., Ng, S.S., Young, A., Ngiow, S.F., Rautela, J., Straube, J., Waddell, N., Blake, S.J., et al. (2017). Tumor immunoevasion by the conversion of effector NK cells into type 1 innate lymphoid cells. Nat. Immunol. *18*, 1004–1015.

22. Ducimetière, L., Lucchiari, G., Litscher, G., Nater, M., Heeb, L., Nuñez, N.G., Wyss, L., Burri, D., Vermeer, M., Gschwend, J., et al. (2021). Conventional NK cells and tissue-resident ILC1s join forces to control liver metastasis. Proc. Natl. Acad. Sci. USA *118*.

23. McFarland, A.P., Yalin, A., Wang, S.Y., Cortez, V.S., Landsberger, T., Sudan, R., Peng, V., Miller, H.L., Ricci, B., David, E., et al. (2021). Multi-tissue single-cell analysis deconstructs the complex programs of mouse natural killer and type 1 innate lymphoid cells in tissues and circulation. Immunity *54*, 1320–1337.e4.

24. Pombo Antunes, A.R., Scheyltjens, I., Lodi, F., Messiaen, J., Antoranz, A., Duerinck, J., Kancheva, D., Martens, L., De Vlaminck, K., Van Hove, H., et al. (2021). Single-cell profiling of myeloid cells in glioblastoma across species and disease stage reveals macrophage competition and specialization. Nat. Neurosci. *24*, 595–610.

25. Wong, K.L., Tai, J.J., Wong, W.C., Han, H., Sem, X., Yeap, W.H., Kourilsky, P., and Wong, S.C. (2011). Gene expression profiling reveals the defining features of the classical, intermediate, and nonclassical human monocyte subsets. Blood *118*, e16–e31.

26. Zhang, Q., Bi, J., Zheng, X., Chen, Y., Wang, H., Wu, W., Wang, Z., Wu, Q., Peng, H., Wei, H., et al. (2018). Blockade of the checkpoint receptor TIGIT prevents NK cell exhaustion and elicits potent anti-tumor immunity. Nat. Immunol. *19*, 723–732.

27. Walzer, T., Chiossone, L., Chaix, J., Calver, A., Carozzo, C., Garrigue-Antar, L., Jacques, Y., Baratin, M., Tomasello, E., and Vivier, E. (2007). Natural killer cell trafficking in vivo requires a dedicated sphingosine 1-phosphate receptor. Nat. Immunol. *8*, 1337–1344.

28. Hertwig, L., Hamann, I., Romero-Suarez, S., Millward, J.M., Pietrek, R., Chanvillard, C., Stuis, H., Pollok, K., Ransohoff, R.M., Cardona, A.E., and Infante-Duarte, C. (2016). CX3CR1-dependent recruitment of mature NK cells into the central nervous system contributes to control autoimmune neuroinflammation. Eur. J. Immunol. *46*, 1984–1996.

29. Yu, M., Su, Z., Huang, X., and Wang, X. (2021). Single-cell sequencing reveals the novel role of Ezh2 in NK cell maturation and function. Front. Immunol. *12*, 724276.

30. Viel, S., Marçais, A., Guimaraes, F.S., Loftus, R., Rabilloud, J., Grau, M., Degouve, S., Djebali, S., Sanlaville, A., Charrier, E., et al. (2016). TGF-beta inhibits the activation and functions of NK cells by repressing the mTOR pathway. Sci. Signal. *9*, ra19.

31. Garcia-Alonso, L., Holland, C.H., Ibrahim, M.M., Turei, D., and Saez-Rodriguez, J. (2019). Benchmark and integration of resources for the estimation of human transcription factor activities. Genome Res. *29*, 1363–1375.

32. Cortez, V.S., Ulland, T.K., Cervantes-Barragan, L., Bando, J.K., Robinette, M.L., Wang, Q., White, A.J., Gilfillan, S., Cella, M., and Colonna, M. (2017). SMAD4 impedes the conversion of NK cells into ILC1-like cells by curtailing non-canonical TGF-beta signaling. Nat. Immunol. *18*, 995–1003.

33. Samson, S.I., Richard, O., Tavian, M., Ranson, T., Vosshenrich, C.A., Colucci, F., Buer, J., Grosveld, F., Godin, I., and Di Santo, J.P. (2003). GATA-3 promotes maturation, IFN-gamma production, and liver-specific homing of NK cells. Immunity *19*, 701–711.

34. Mace, E.M., Hsu, A.P., Monaco-Shawver, L., Makedonas, G., Rosen, J.B., Dropulic, L., Cohen, J.I., Frenkel, E.P., Bagwell, J.C., Sullivan, J.L., et al. (2013). Mutations in GATA2 cause human NK cell deficiency with specific loss of the CD56(bright) subset. Blood *121*, 2669–2677.

35. Li, K., Wu, Y., Li, Y., Yu, Q., Tian, Z., Wei, H., and Qu, K. (2020). Landscape and dynamics of the transcriptional regulatory network during natural killer cell differentiation. Genomics Proteomics Bioinformatics *18*, 501–515.

36. Constam, D.B., Philipp, J., Malipiero, U.V., ten Dijke, P., Schachner, M., and Fontana, A. (1992). Differential expression of transforming growth factor-beta 1, -beta 2, and -beta 3 by glioblastoma cells, astrocytes, and microglia. J. Immunol. *148*, 1404–1410.

37. Shaim, H., Shanley, M., Basar, R., Daher, M., Gumin, J., Zamler, D.B., Uprety, N., Wang, F., Huang, Y., Gabrusiewicz, K., et al. (2021). Targeting the αv integrin/TGF-β axis improves natural killer cell function against glioblastoma stem cells. J. Clin. Invest. *131*.

38. Noy, R., and Pollard, J.W. (2014). Tumor-associated macrophages: from mechanisms to therapy. Immunity *41*, 49–61.

39. Bowman, R.L., Klemm, F., Akkari, L., Pyonteck, S.M., Sevenich, L., Quail, D.F., Dhara, S., Simpson, K., Gardner, E.E., Iacobuzio-Donahue, C.A., et al. (2016). Macrophage ontogeny underlies differences in tumor-specific education in brain malignancies. Cell Rep. *17*, 2445–2459.

40. Molgora, M., Esaulova, E., Vermi, W., Hou, J., Chen, Y., Luo, J., Brioschi, S., Bugatti, M., Omodei, A.S., Ricci, B., et al. (2020). TREM2 modulation remodels the tumor myeloid landscape enhancing anti-PD-1 immunotherapy. Cell *182*, 886–900.e17.

41. Katzenelenbogen, Y., Sheban, F., Yalin, A., Yofe, I., Svetlichnyy, D., Jaitin, D.A., Bornstein, C., Moshe, A., Keren-Shaul, H., Cohen, M., et al. (2020). Coupled scRNA-seq and intracellular protein activity reveal an immunosuppressive role of TREM2 in cancer. Cell *182*, 872–885.e19.

42. Park, M.D., Reyes-Torres, I., LeBerichel, J., Hamon, P., LaMarche, N.M., Hegde, S., Belabed, M., Troncoso, L., Grout, J.A., Magen, A., et al. (2023). TREM2 macrophages drive NK cell paucity and dysfunction in lung cancer. Nat. Immunol. *24*, 792–801.

43. Mounce, B.C., Poirier, E.Z., Passoni, G., Simon-Loriere, E., Cesaro, T., Prot, M., Stapleford, K.A., Moratorio, G., Sakuntabhai, A., Levraud, J.P., and Vignuzzi, M. (2016). Interferon-induced spermidine-spermine acetyltransferase and polyamine depletion restrict Zika and chikungunya viruses. Cell Host Microbe *20*, 167–177.

44. Qin, R., Ren, W., Ya, G., Wang, B., He, J., Ren, S., Jiang, L., and Zhao, S. (2023). Role of chemokines in the crosstalk between tumor and tumor-associated macrophages. Clin. Exp. Med. *23*, 1359–1373.

45. Davidson, S., Efremova, M., Riedel, A., Mahata, B., Pramanik, J., Huuhtanen, J., Kar, G., Vento-Tormo, R., Hagai, T., Chen, X., et al. (2020). Single-cell RNA sequencing reveals a dynamic stromal niche that supports tumor growth. Cell Rep. *31*, 107628.

46. Lewis, J.S., Landers, R.J., Underwood, J.C., Harris, A.L., and Lewis, C.E. (2000). Expression of vascular endothelial growth factor by macrophages is up-regulated in poorly vascularized areas of breast carcinomas. J. Pathol. *192*, 150–158.

47. Ceci, C., Atzori, M.G., Lacal, P.M., and Graziani, G. (2020). Role of VEGFs/VEGFR-1 signaling and its inhibition in modulating tumor invasion: experimental evidence in different metastatic cancer models. Int. J. Mol. Sci. *21*.

48. Ma, G., Pan, P.Y., Eisenstein, S., Divino, C.M., Lowell, C.A., Takai, T., and Chen, S.H. (2011). Paired immunoglobin-like receptor-B regulates the suppressive function and fate of myeloid-derived suppressor cells. Immunity *34*, 385–395.

49. Zhou, T., Damsky, W., Weizman, O.E., McGeary, M.K., Hartmann, K.P., Rosen, C.E., Fischer, S., Jackson, R., Flavell, R.A., Wang, J., et al. (2020). IL-18BP is a secreted immune checkpoint and barrier to IL-18 immunotherapy. Nature *583*, 609–614.

50. Hiroi, M., Sakaeda, Y., Yamaguchi, H., and Ohmori, Y. (2013). Anti-inflammatory cytokine interleukin-4 inhibits inducible nitric oxide synthase gene expression in the mouse macrophage cell line RAW264.7 through the repression of octamer-dependent transcription. Mediators Inflamm. *2013*, 369693.

51. Xu, F., Kang, Y., Zhang, H., Piao, Z., Yin, H., Diao, R., Xia, J., and Shi, L. (2013). Akt1-mediated regulation of macrophage polarization in a murine model of Staphylococcus aureus pulmonary infection. J. Infect. Dis. *208*, 528–538.

52. Platanitis, E., Demiroz, D., Schneller, A., Fischer, K., Capelle, C., Hartl, M., Gossenreiter, T., Müller, M., Novatchkova, M., and Decker, T. (2019). A molecular switch from STAT2-IRF9 to ISGF3 underlies interferon-induced gene transcription. Nat. Commun. *10*, 2921.

53. Yu, W., Wang, X., Zhao, J., Liu, R., Liu, J., Wang, Z., Peng, J., Wu, H., Zhang, X., Long, Z., et al. (2020). Stat2-Drp1 mediated mitochondrial mass increase is necessary for pro-inflammatory differentiation of macrophages. Redox Biol. *37*, 101761.

54. Corzo, C.A., Condamine, T., Lu, L., Cotter, M.J., Youn, J.I., Cheng, P., Cho, H.I., Celis, E., Quiceno, D.G., Padhya, T., et al. (2010). HIF-1alpha regulates function and differentiation of myeloid-derived suppressor cells in the tumor microenvironment. J. Exp. Med. *207*, 2439–2453.

55. Luan, B., Yoon, Y.S., Le Lay, J., Kaestner, K.H., Hedrick, S., and Montminy, M. (2015). CREB pathway links PGE2 signaling with macrophage polarization. Proc. Natl. Acad. Sci. USA *112*, 15642–15647.

56. Ou, D.L., Chen, C.W., Hsu, C.L., Chung, C.H., Feng, Z.R., Lee, B.S., Cheng, A.L., Yang, M.H., and Hsu, C. (2021). Regorafenib enhances antitumor immunity via inhibition of p38 kinase/Creb1/Klf4 axis in tumor-associated macrophages. J. Immunother. Cancer *9*, e001657.

57. Kobayashi, E.H., Suzuki, T., Funayama, R., Nagashima, T., Hayashi, M., Sekine, H., Tanaka, N., Moriguchi, T., Motohashi, H., Nakayama, K., and Yamamoto, M. (2016). Nrf2 suppresses macrophage inflammatory response by blocking proinflammatory cytokine transcription. Nat. Commun. *7*, 11624.

58. Zamanian-Daryoush, M., Lindner, D., Tallant, T.C., Wang, Z., Buffa, J., Klipfell, E., Parker, Y., Hatala, D., Parsons-Wingerter, P., Rayman, P., et al. (2013). The cardioprotective protein apolipoprotein A1 promotes potent anti-tumorigenic effects. J. Biol. Chem. *288*, 21237–21252.

59. Moraes, L.A., Kar, S., Foo, S.L., Gu, T., Toh, Y.Q., Ampomah, P.B., Sachaphibulkij, K., Yap, G., Zharkova, O., Lukman, H.M., et al. (2017). Annexin-A1 enhances breast cancer growth and migration by promoting alternative macrophage polarization in the tumour microenvironment. Sci. Rep. *7*, 17925.

60. Batlle, E., and Massagué, J. (2019). Transforming growth factor-beta signaling in immunity and cancer. Immunity *50*, 924–940.

61. Fontana, M.F., Baccarella, A., Pancholi, N., Pufall, M.A., Herbert, D.R., and Kim, C.C. (2015). JUNB is a key transcriptional modulator of macrophage activation. J Immunol *194*, 177–186.

62. Xie, G., Cheng, T., Lin, J., Zhang, L., Zheng, J., Liu, Y., Xie, G., Wang, B., and Yuan, Y. (2018). Local angiotensin II contributes to tumor resistance to checkpoint immunotherapy. J. Immunother. Cancer *6*, 88.

63. Little, A.C., Pathanjeli, P., Wu, Z., Bao, L., Goo, L.E., Yates, J.A., Oliver, C.R., Soellner, M.B., and Merajver, S.D. (2019). IL-4/IL-13 stimulated macrophages enhance breast cancer invasion via rho-GTPase regulation of synergistic VEGF/CCL-18 signaling. Front. Oncol. *9*, 456.

64. Bune, A.J., Hayman, A.R., Evans, M.J., and Cox, T.M. (2001). Mice lacking tartrate-resistant acid phosphatase (Acp 5) have disordered macrophage inflammatory responses and reduced clearance of the pathogen, Staphylococcus aureus. Immunology *102*, 103–113.

65. Räisänen, S.R., Alatalo, S.L., Ylipahkala, H., Halleen, J.M., Cassady, A.I., Hume, D.A., and Väänänen, H.K. (2005). Macrophages overexpressing tartrate-resistant acid phosphatase show altered profile of free radical production and enhanced capacity of bacterial killing. Biochem. Biophys. Res. Commun. *331*, 120–126.

66. Orecchioni, M., Ghosheh, Y., Pramod, A.B., and Ley, K. (2019). Macrophage polarization: different gene signatures in M1(LPS+) vs. classically and M2(LPS-) vs. alternatively activated macrophages. Front. Immunol. *10*, 1084.

67. How, J., Brown, J.R., Saylor, S., and Rimm, D.L. (2014). Macrophage expression of tartrate-resistant acid phosphatase as a prognostic indicator in colon cancer. Histochem. Cell Biol. *142*, 195–204.

68. Hannemann, N., Cao, S., Eriksson, D., Schnelzer, A., Jordan, J., Eberhardt, M., Schleicher, U., Rech, J., Ramming, A., Uebe, S., et al. (2019). Transcription factor Fra-1 targets arginase-1 to enhance macrophage-mediated inflammation in arthritis. J. Clin. Invest. *129*, 2669–2684.

69. Biswas, S.K., and Lewis, C.E. (2010). NF-κB as a central regulator of macrophage function in tumors. J. Leukoc. Biol. *88*, 877–884.

70. Miyata, Y., Fukuhara, A., Otsuki, M., and Shimomura, I. (2013). Expression of activating transcription factor 2 in inflammatory macrophages in obese adipose tissue. Obesity (Silver Spring) *21*, 731–736.

71. Sica, A., and Mantovani, A. (2012). Macrophage plasticity and polarization: in vivo veritas. J. Clin. Invest. *122*, 787–795.

72. McGettrick, A.F., and O'Neill, L.A.J. (2020). The role of HIF in immunity and inflammation. Cell Metab. *32*, 524–536.

73. Wagner, A., Wang, C., Fessler, J., DeTomaso, D., Avila-Pacheco, J., Kaminski, J., Zaghouani, S., Christian, E., Thakore, P., Schellhaass, B., et al. (2021). Metabolic modeling of single Th17 cells reveals regulators of autoimmunity. Cell *184*, 4168–4185.e21.

74. Kohli, K., Pillarisetty, V.G., and Kim, T.S. (2022). Key chemokines direct migration of immune cells in solid tumors. Cancer Gene Ther. *29*, 10–21.

75. Kim, B.G., Malek, E., Choi, S.H., Ignatz-Hoover, J.J., and Driscoll, J.J. (2021). Novel therapies emerging in oncology to target the TGF-beta pathway. J. Hematol. Oncol. *14*, 55.

76. Nie, Y., Huang, H., Guo, M., Chen, J., Wu, W., Li, W., Xu, X., Lin, X., Fu, W., Yao, Y., et al. (2019). Breast phyllodes tumors recruit and repolarize

tumor-associated macrophages via secreting CCL5 to promote malignant progression, which can be inhibited by CCR5 inhibition therapy. Clin. Cancer Res. *25*, 3873–3886.

77. Ntanasis-Stathopoulos, I., Fotiou, D., and Terpos, E. (2020). CCL3 signaling in the tumor microenvironment. Adv. Exp. Med. Biol. *1231*, 13–21.
78. Novak, M., Koprivnikar Krajnc, M., Hrastar, B., Breznik, B., Majc, B., Mlinar, M., Rotter, A., Porčnik, A., Mlakar, J., Stare, K., et al. (2020). CCR5-mediated signaling is involved in invasion of glioblastoma cells in its microenvironment. Int. J. Mol. Sci. *21*, 4199.
79. Jiao, X., Nawab, O., Patel, T., Kossenkov, A.V., Halama, N., Jaeger, D., and Pestell, R.G. (2019). Recent advances targeting CCR5 for cancer and its role in immuno-oncology. Cancer Res. *79*, 4801–4807.
80. Neumann, J.v. (1955). Method in the physical sciences, Collected Works (New York: The Unity of Knowledge, Doubleday), pp. 157–164.
81. Soskic, B., Cano-Gamez, E., Smyth, D.J., Ambridge, K., Ke, Z., Matte, J.C., Bossini-Castillo, L., Kaplanis, J., Ramirez-Navarro, L., Lorenc, A., et al. (2022). Immune disease risk variants regulate gene expression dynamics during $CD4^+$ T cell activation. Nat. Genet. *54*, 817–826.
82. Alda-Catalinas, C., Bredikhin, D., Hernando-Herraez, I., Santos, F., Kubinyecz, O., Eckersley-Maslin, M.A., Stegle, O., and Reik, W. (2020). A single-cell transcriptomics CRISPR-activation screen identifies epigenetic regulators of the zygotic genome activation program. Cell Syst. *11*, 25–41.e9.
83. Sanmarco, L.M., Chao, C.C., Wang, Y.C., Kenison, J.E., Li, Z., Rone, J.M., Rejano-Gordillo, C.M., Polonio, C.M., Gutierrez-Vazquez, C., Piester, G., et al. (2022). Identification of environmental factors that promote intestinal inflammation. Nature *611*, 801–809.
84. Kuhn, M., Santinha, A.J., and Platt, R.J. (2021). Moving from in vitro to in vivo CRISPR screens. Gene Genome Edit. *2*, 100008.
85. Galli, E., Friebel, E., Ingelfinger, F., Unger, S., Núñez, N.G., and Becher, B. (2019). The end of omics? High dimensional single cell analysis in precision medicine. Eur. J. Immunol. *49*, 212–220.
86. Mathieson, T., Franken, H., Kosinski, J., Kurzawa, N., Zinn, N., Sweetman, G., Poeckel, D., Ratnu, V.S., Schramm, M., Becher, I., et al. (2018). Systematic analysis of protein turnover in primary cells. Nat. Commun. *9*, 689.
87. Aibar, S., González-Blas, C.B., Moerman, T., Huynh-Thu, V.A., Imrichova, H., Hulselmans, G., Rambow, F., Marine, J.C., Geurts, P., Aerts, J., et al. (2017). SCENIC: single-cell regulatory network inference and clustering. Nat. Methods *14*, 1083–1086.
88. Tang, Z., Li, C., Kang, B., Gao, G., Li, C., and Zhang, Z. (2017). GEPIA: a web server for cancer and normal gene expression profiling and interactive analyses. Nucleic Acids Res. *45*, W98–W102.
89. Jiang, H., Gomez-Manzano, C., Aoki, H., Alonso, M.M., Kondo, S., McCormick, F., Xu, J., Kondo, Y., Bekele, B.N., Colman, H., et al. (2007). Examination of the therapeutic potential of Delta-24-RGD in brain tumor stem cells: role of autophagic cell death. J. Natl. Cancer Inst. *99*, 1410–1414.
90. Pollard, S.M., Yoshikawa, K., Clarke, I.D., Danovi, D., Stricker, S., Russell, R., Bayani, J., Head, R., Lee, M., Bernstein, M., et al. (2009). Glioma stem cell lines expanded in adherent culture have tumor-specific phenotypes and are suitable for chemical and genetic screens. Cell Stem Cell *4*, 568–580.
91. Look, T., Puca, E., Bühler, M., Kirschenbaum, D., De Luca, R., Stucchi, R., Ravazza, D., Di Nitto, C., Roth, P., Katzenelenbogen, Y., et al. (2023). Targeted delivery of tumor necrosis factor in combination with CCNU induces a T cell-dependent regression of glioblastoma. Sci. Transl. Med. *15*, eadf2281.
92. Jaitin, D.A., Kenigsberg, E., Keren-Shaul, H., Elefant, N., Paul, F., Zaretsky, I., Mildner, A., Cohen, N., Jung, S., Tanay, A., and Amit, I. (2014). Massively parallel single-cell RNA-seq for marker-free decomposition of tissues into cell types. Science *343*, 776–779.
93. Keren-Shaul, H., Kenigsberg, E., Jaitin, D.A., David, E., Paul, F., Tanay, A., and Amit, I. (2019). MARS-seq2.0: an experimental and analytical pipeline for indexed sorting combined with single-cell RNA sequencing. Nat. Protoc. *14*, 1841–1862.
94. Stirling, D.R., Swain-Bowden, M.J., Lucas, A.M., Carpenter, A.E., Cimini, B.A., and Goodman, A. (2021). CellProfiler 4: improvements in speed, utility and usability. BMC Bioinformatics *22*, 433.
95. Xie, K., Liu, Z., Chen, N., and Chen, T. (2021). redPATH: reconstructing the pseudo development time of cell lineages in single-cell RNA-seq data and applications in cancer. Genomics Proteomics Bioinformatics *19*, 292–305.
96. Tirosh, I., Izar, B., Prakadan, S.M., Wadsworth, M.H., 2nd, Treacy, D., Trombetta, J.J., Rotem, A., Rodman, C., Lian, C., Murphy, G., et al. (2016). Dissecting the multicellular ecosystem of metastatic melanoma by single-cell RNA-seq. Science *352*, 189–196.
97. Hao, Y., Hao, S., Andersen-Nissen, E., Mauck, W.M., 3rd, Zheng, S., Butler, A., Lee, M.J., Wilk, A.J., Darby, C., Zager, M., et al. (2021). Integrated analysis of multimodal single-cell data. Cell *184*, 3573–3587.e29.
98. Love, M.I., Huber, W., and Anders, S. (2014). Moderated estimation of fold change and dispersion for RNA-seq data with DESeq2. Genome Biol. *15*, 550.
99. Browaeys, R., Saelens, W., and Saeys, Y. (2020). NicheNet: modeling intercellular communication by linking ligands to target genes. Nat. Methods *17*, 159–162.
100. Wolf, F.A., Angerer, P., and Theis, F.J. (2018). SCANPY: large-scale single-cell gene expression data analysis. Genome Biol. *19*, 15.
101. Pierre, B., Justin, H., Adam, G., Michael, I.J., Elham, A., and Nir, Y. (2022). Deep generative modeling for quantifying sample-level heterogeneity in single-cell omics. bioRxiv. https://www.biorxiv.org/content/10.1101/2022.10.04.510898v1.
102. Bergen, V., Lange, M., Peidli, S., Wolf, F.A., and Theis, F.J. (2020). Generalizing RNA velocity to transient cell states through dynamical modeling. Nat. Biotechnol. *38*, 1408–1414.
103. Haghverdi, L., Büttner, M., Wolf, F.A., Buettner, F., and Theis, F.J. (2016). Diffusion pseudotime robustly reconstructs lineage branching. Nat. Methods *13*, 845–848.
104. Qiu, X., Hill, A., Packer, J., Lin, D., Ma, Y.A., and Trapnell, C. (2017). Single-cell mRNA quantification and differential analysis with census. Nat. Methods *14*, 309–315.
105. Qiu, X., Mao, Q., Tang, Y., Wang, L., Chawla, R., Pliner, H.A., and Trapnell, C. (2017). Reversed graph embedding resolves complex single-cell trajectories. Nat. Methods *14*, 979–982.
106. Setty, M., Kiseliovas, V., Levine, J., Gayoso, A., Mazutis, L., and Pe'er, D. (2019). Characterization of cell fate probabilities in single-cell data with Palantir. Nat. Biotechnol. *37*, 451–460.
107. Robrecht, C., Wouter, S., Dorine, S., Simon, T., Sophie, J., Martin, G., Bart, L., Katleen De, P., and Yvan, S. (2016). SCORPIUS improves trajectory inference and identifies novel modules in dendritic cell development. bioRxiv. https://www.biorxiv.org/content/10.1101/079509v2.

STAR★METHODS

KEY RESOURCES TABLE

REAGENT or RESOURCE	SOURCE	IDENTIFIER
Antibodies		
Rat anti-CD45 clone 30F11 PE	Biolegend	#Cat 103106;
Rat anti-CD45 clone 30F11 BV711	BD Biosciences	#Cat 563709; RRID: AB_2687455
Rat anti-CD45 clone 30F11 BUV737	BD Biosciences	#Cat 748371; RRID: AB_2872790
Rat anti-CD45 clone 30F11 BB515	BD Biosciences	#Cat 564590; RRID: AB_2738857
Rat anti-CD45 clone 30F11 APC	BD Biosciences	#Cat 559864; RRID: AB_398672
Rat anti-CD45 clone 30F11 BV421	BD Biosciences	#Cat 563890; RRID: AB_2651151
Anti murine TREM2 clone 178	Provided by Marco Colonna, WUSTL	N/A
Anti human ILT1 clone 135.5	Provided by Marco Colonna, WUSTL	N/A
Anti P2RY12 clone S16007D Alexa Fluor 647	Biolegend	#Cat 848017;RRID: AB_2941635
Anti CD11b clone M1/70 BV605	Biolegend	#Cat 101237;RRID: AB_11126744
Anti CD31 clone MEC13.3 APC	Biolegend	#Cat 102509; RRID: AB_312916
Anti F4/80 clone BM8 APC-eFluor780	eBioscience	#Cat 47480182;RRID: AB_2735036
TruStain FcX, anti CD16/32 clone 93	Biolegend	#Cat 101319;RRID: AB_1574973
Anti TGF-β 123 clone 1D11	R&D	#Cat MAB1835-500;RRID: AB_357931
Anti CD107a clone H4A3 PE-CF594	BD Biosciences	Cat# 562628;RRID: AB_2737686
Anti CD56 clone HCD56 BV605	Biolegend	Cat# 318334; RRID: AB_2561912
Anti IFNγ clone B27 v450	BD Biosciences	Cat# 560372; RRID: AB_1645595
Anti TNFα clone Mab11 Alexa700	BD Biosciences	Cat# 557996; RRID: AB_396978
Anti CD3 clone SK7 APC-Cy7	Biolegend	Cat#344818; RRID: AB_10645474
Anti LY-6C clone HK1.4 PerCP/Cy5.5	Biolegend	#Cat 128012; RRID: AB_1659241
Anti TCR b chain H57-597 APC/Cy7	Biolegend	#Cat 109219;RRID: AB_893626
Anti CD45.1 clone A20 Alexa Fluor 488	Biolegend	#Cat 110717; RRID: AB_492863
Anti CD19 clone 6D5 PE/Cy7	Biolegend	#Cat 115520; RRID: AB_313655
Biological samples		
Human GSC cell lines	MD Anderson Cancer Center	N/A
Human NK cells	MD Anderson Cancer Center	N/A
Chemicals, peptides, and recombinant proteins		
Recombinant human TGF- β	Peprotech	Cat# 100-21C-10
MCSF	Peprotech	Cat# 300-25-100
L-glutamine	Sartorius	Cat# 030201B
Non Essential Amino Acids	Biological Industries	Cat# 013401B
Mercaptoethanol	Gibco	Cat# 35310-010
Sodium pyruvate 1mM	Sartorius	Cat# 03-042-1B
Penicillin-streptomycin	Biological Industries	Cat# 03-031-1B;
Fetal bovine serum (HyClone)	GE	Cat# SH30071.03
Albumine Bovine, Fraction V	MP-Biomedicals	Cat# 9048-46-8
Ficoll-Paque PLUS	Sigma-Aldrich	Cat# 17-1440-03
Brefeldin A	Sigma-Aldrich	Cat# B7651
PMA	Sigma-Aldrich	Cat# P8139
Ionomycin	Sigma-Aldrich	Cat# I9657
Live/dead aqua viability dye	Thermo Fisher Scientific	Cat# L34957
BD Cytofix/Cytoperm™ Fixation/Permeabilization Kit	BD Biosciences	Cat# 554714
Percoll	Sigma-Aldrich	Cat# GE17089101

(*Continued on next page*)

Continued

REAGENT or RESOURCE	SOURCE	IDENTIFIER
EDTA 0.5M in water, pH 8.0	Sigma-Aldrich	Cat# 03690
4',6-Diamidino-2-Phenylindole, Dilactate (DAPI)	Biolegend	Cat# 422801
Dithiotreithol, 0.1M (SuperScript II)	Thermo Fisher Scientific	Cat# 18064022
RBC lysis solution	Sigma	Cat# R7757
Monensin, GolgiStopTM	BD Biosciences	Cat# 554724
Murine GM-CSF	PeproTech	Cat# 315-03-20
ACK Lysing Buffer	Thermo Fisher Scientific	Cat# A1049201
Collagenase IV	Worthington	Cat# LS004188
DNase	Roche	Cat# 10104159001
Deposited data		
Zman-seq scRNAseq raw data, brain tumor and peripheral organs	NCBI Gene Expression Omnibus	GEO: GSE232040
Human scRNAseq data from brain tumor	Pombo Antunes et al.[24]	GEO: GSE163120
TCGA human cancer database	Tang et al.[87]	http://gepia.cancer-pku.cn
Experimental models: Cell lines		
Mouse: GL261 glioblastoma	Provided by the laboratory of Tobias Weiss[88]	CVCL_Y003
Human: K562 erythroleukemia	ATCC	CCL-243; CVCL_0004
Experimental models: Organisms/strains		
Mouse: C57BL/6/WT	Harlan	N/A
Mouse: C57BL/6 Ub-GFP	The Jackson Laboratory	IMSR_JAX:004353
Mouse: C57BL/6/SJL CD45.1	The Jackson Laboratory	IMSR_JAX:002014
Oligonucleotides		
qPCR primer Actb left: GGAGGGGGTTGAGGTGTT	This paper	N/A
qPCR primer Actb right: TGTGCACTTTTATTGGTCTCAAG	This paper	N/A
Software and algorithms		
ZmanR package	This paper	https://github.com/kenxie7/ZmanR
Python version 3.8.16	Python Software Foundation	https://www.python.org/
R version 4.1.0	The R Foundation	http://www.r-project.org/
FlowJo software	FlowJo, LLC	https://www.flowjo.com/
ImageJ Version 1.53t	National Institutes of Health	https://imagej.net/ij/index.html
CellProfiler version 4.2.5	Broad Institute	https://cellprofiler.org
Other		
MARS-seq reagents	Jaitin et al.[89] and Keren-Shaul et al.[90]	N/A

RESOURCE AVAILABILITY

Lead contact

Further information and requests for resources and reagents should be directed to and will be fulfilled by the lead contact, Ido Amit (ido.amit@weizmann.ac.il).

Materials availability

This study did not generate new unique reagents.

Data and code availability

- Single-cell RNA-seq data have been deposited at GEO and are publicly available as of the date of publication. Accession numbers are listed in the key resources table. All original code has been deposited at GitHub and is publicly available as of the date of publication. URL is listed in the key resources table. Microscopy data reported in this paper will be shared by the lead contact upon request.

- This paper analyzes existing, publicly available data. These accession numbers for the datasets are listed in the key resources table, or are available at http://gepia.cancer-pku.cn.
- Any additional information required to reanalyze the data reported in this paper is available from the lead contact upon request.

EXPERIMENTAL MODEL AND STUDY PARTICIPANT DETAILS

Cell lines

GL261 mouse glioma cells (kindly provided by the laboratory of T. Weiss, University Hospital Zurich)[88] were grown in Dulbecco's Modified Eagle Medium (DMEM, Gibco, 41965-039) at 37° C with 5% CO_2, supplemented with 1% penicillin-streptomycin (Biological Industries, 03-031-1B), 2mM L-glutamine (Sartorius, 03-020-1B), 1mM sodium pyruvate (Sartorius, 03-042-1B) and 10% heat inactivated fetal bovine serum (GE, Cat# SH30071.03).

Mouse primary bone marrow derived macrophages (BMDMs)

Primary bone marrow cells from female C57BL/6 mouse were cultured with C10 medium containing RPMI medium supplemented with 10% FBS (GE, Cat# SH30071.03), 1mM sodium pyruvate (Sartorius, Cat# 03-042-1B), 1% x100 non-essential amino acids (Biological Industries, Cat# 013401B), 10mM HEPES buffer, 2mM L-glutamine (Sartorius, Cat# 030201B) and 50μM b-mercaptoethanol (Gibco, Cat# 35310-010), 30 ng/ml MCSF (Peprotech, Cat# 300-25-100), maintained at 37°C and 5% CO_2.

Mouse models

For all Zman-seq experiments female (8–13 weeks old) wildtype mice (C57BL/6) (Harlan) were housed in the Weizmann Institute animal facility under pathogen-free conditions and 12-h light/12-h dark cycle. Food and water was provided ad libitum. For antibody decay measurements C57BL/6 Ub-GFP transgenic mice (Strain #004353) and B6.SJL mice (Strain #033076) were used.

All experiments were conducted as approved by the Institutional Animal Care and Use Committee. Mice were monitored daily for 3 days after tumor implantation. Tumor bearing mice were sacrificed before (<14 days post implantation) the development of symptoms for scRNAseq experiments.

METHOD DETAILS

Animal treatments

Glioma-bearing mice were treated intraperitoneally (i.p.) with aTREM2 antibody (clone 178; Fc-mutated recombinant mAb, 200μg/mouse) on day 2 and 7.[40] Anti-hILT1 (clone 135.5; Fc-mutated recombinant mAb specific for human ILT1, a receptor absent in mice) was used as a control (200 μg/mouse).

Brain tumor implantation

Eleven-week-old female mice were anesthetized with isoflurane (Isoflurane, USP Terrell, Piramal) (3-4% induction, 1.5-2% maintenance), received local 2 mg/kg lidocaine (Vetmarket 2%, 162097) and systemic 0.05 mg/kg buprenorphine (Bupaq, 0.3mg/ml, Richter Pharma) analgesia. Mice were intracerebrally injected with $2x10^4$ GL261 cells in 2μl PBS in the right anterior striatum (coordinates from Bregma: +0.5 mm antero-posterior, +2.2 mm medio-lateral, -3.5 mm dorso-ventral). Mice were kept on a heating pad during the procedure and until mice were awake and mobile. After surgery mice were monitored and treated with meloxicam 5mg/kg (Loxicom, 5 mg/ml, Norbrook) subcutaneously daily, for three days.

In vivo time stamping

Mice were briefly anesthetized with isoflurane (3-4%) and were injected with 100 μl of fluorescent antibody solution intravenously (containing 1.2 or 4 μg antibody corresponding to 60 μg/kg or 200 μg/kg body weight (bw) respectively). Time stamping was done with CD45 antibodies, clone 30-F11 with following fluorophores: PE (Biolegend, Cat# 103106), BB515 (BD Biosciences, Cat# 564590), BUV737 (BD Biosciences, Cat# 748371), BV711 (BD Biosciences, Cat# 563709). We consistently observed a broad range of fluorescence intensities of PBMC cells for all fluorophores, already 15 minutes after *in vivo* CD45-antibody injection.

In order to calibrate antibody concentrations for *in vivo* timestamping we injected 20, 60 and 200 ug/kg bw CD45-PE labeled antibodies and analyzed the PBMCs 15 minutes later via FACS (Figures 1B and S1A).

We established at what rate injected CD45 antibodies become unavailable for binding CD45 in the blood by sampling the blood (50 μl) of mice 5, 15, 30, 60, and 90 minutes after injecting 200 ug/kg bw CD45-PE. We indirectly measured the amount of unbound CD45-PE antibody by mixing the samples with 50 μl blood from a GFP-mouse for 15 minutes, followed by washing and measuring the PE emission of GFP^+ cells via FACS (Figures 1C and S1B).

Estimating the *in vivo* labeling decay

The decay of anti-CD45-PE antibody from stained cells (Figure S1F) was measured by transferring CD45-PE stained CD45.1+ cells ($2x10^6$ in 100 μl PBS) from congenic mice (B6.SJL) to CD45.2 mice. Three mice received CD45-PE stained CD45.1 cells, one control

mouse received CD45.1 cells without PE stain, one mouse did not receive cell transfer. CD45.1 PBMCs were isolated from the blood of 5 female mice with Ficoll density gradient and were stained for 20 minutes on 4°C with CD45-PE antibody (Biolegend, Cat# 103106, 1:100). At 4, 8, 24, 48, 96, 144 hours after cell transfer, 100 μl of blood was drawn. Red blood cells were lysed with RBC lysis solution (Sigma, Cat# R7757) washed with FACS buffer and stained with antibodies against CD45.1 (Biolegend, Alexa 488, clone A20, Cat# 110717), CD11b (Biolegend, BV605, clone M1/70, Cat#101237), CD19 (Biolegend, PE/Cy7, clone 6D5, Cat# 313655), TCR b chain (BioLegend, APC/Cy7, clone H57-597, Cat #109219), LY-6c (Biolegend, PerCP/Cy5.5, clone HK1.4, Cat# 128012) and DAPI live/dead stain. Cells were washed with FACS buffer and measured with BD LSR II flow cytometer. Data was analyzed with FlowJo and R.

Flow cytometry analysis of tumor infiltrating and resident CD45$^+$ cells

We tested for how long *in vivo* stained leukocytes can be detected in the tumor by injecting mice with distinct fluorescent CD45 antibodies 60, 48, 36 and 24 hours (PE, BV711, BB515, BUV737 respectively) before mice were sacrificed (Figures 1E and S1D). Mice were transcardially perfused with PBS to wash out the blood. Tumors were dissociated into single cell suspensions, stained for CD45-APC (BD Biosciences, Cat# 559864) and were recorded with BD Symphony 6 flow cytometer. To test whether microglia gets stained by 48, 36, 24 and 12 hour CD45 time stamping, tumor bearing hemispheres were dissociated into single cells and stained 1:100 with CD45-BV421 (BD Biosciences, #Cat 563890), CD11b-BV605 (Biolegend, Cat# 101237), P2RY12-Alexa647 (Biolegend, Cat# 848017), F4/80-APC/eFluor780 (eBioscience, Cat# 47480182), LY6C-PerCP/Cy5.5 (Biolegend, #Cat 128012) (Figures 1F and S1E) and recorded with BD Symphony 6. Data was analyzed with Flowjo and R.

Isolation and *in vitro* treatment of BMDMs

Bone marrow was isolated from a 8-weeks-old female C57BL/6 mouse by flushing the femora and tibiae with C10 culture medium using a 21-gauge needle. The suspension was filtered through a 70-μm cell strainer. Cells were centrifuged at 350 xg for 5 minutes at 4°C. Cells were resuspended in red blood cell lysis solution and incubated for 5 minutes at room temperature, followed by washing and resuspension in C10 medium. Cells were then cultured by plating 150k cells per well (12-well non-tissue culture treated plates) in 1 ml of C10 supplemented with 30 ng/ml human MCSF (Peprotech, Cat #300-25-100). On Day 2 and 5, the medium was replaced by regular C10 medium or one of two preparations of conditioned medium (a 3:1 or 6:1 mixture C10 medium with GL261 supernatant collected and filtered two days after splitting GL261 cell cultures). Cells were treated with 0.01 ug/ml aTREM2 antibody or 0.01 ug/ml isotype control (anti-hILT1) antibody or left untreated. On day 7, cells were washed with PBS and detached with accutase for 15 minutes followed by FACS sorting into MARS-seq capture plates for scRNAseq. For TGF-β treatment experiment, BMDMs were stimulated on day 6 with 20 ng/ml recombinant human TGF-β (Peprotech, Cat# 100-21C-10) and harvested on day 7.

PBMC isolation and FACS analysis

Fresh mouse blood samples were purified via sterile density gradient centrifugation (Ficoll-Paque (GE Healthcare Life Sciences)) at a 1:1 ratio. Centrifugation (500 g, 25 min) was performed at 10°C, and the mononuclear cells were carefully aspirated and washed with ice-cold FACS buffer, followed by washing with ice-cold FACS buffer and staining with CD45-APC and DAPI. Cells were filtered through a 70 μm cell strainer and measured on a BD FACS Symphony 6 (BD Biosciences), data was analyzed with FlowJo and R.

In vitro human NK cell suppression assays

Glioma stem cells (GSCs) were obtained from primary patient samples as previously described.[91,92] GSCs and magnetically purified (Miltenyi) healthy control PBMC NK cells were co-cultured in a 1:1 ratio in the presence or absence of anti–TGF-β 123 (5 μg/ml) (clone 1D11; cat# MAB1835-500, R&D). After 48 hours, K562 target cells (ATCC CCL-243, human erythroleukemia) were added at an optimized effector:target ratio of 5:1 together with CD107a PE-CF594 (clone H4A3; cat# 562628, BD Biosciences), monensin (BD GolgiStopTM, BD Biosciences) and BFA (Brefeldin A, Sigma-Aldrich, Cat# B7651). For negative control, NK cells were incubated without targets while for positive control they were stimulated with PMA (50 ng/mL, Sigma-Aldrich, Cat# P8139) and ionomycin (2 mg/mL, Sigma-Aldrich, Cat# I9657) to directly activate PKC. Cells were collected, washed and stained with a live/dead-aqua viability dye (Thermo Fisher Scientific, cat# L34957) and surface antibodies against CD3-APC-Cy7 (clone SK7; cat# 344818, Biolegend) and CD56-BV605 (clone HCD56; cat# 318334, Biolegend) and then fixed, permeabilized (BD Biosciences, Cat# 554714) and stained with IFN-γ-v450 (clone B27; cat# 560372) and TNF-α Alexa700 (clone MAb11; cat# 557996) (BD Biosciences) antibodies for 30 minutes before washed. The data were acquired using LSRFortessa instrument (BD Biosciences) and analyzed using FlowJo software (FlowJo LLC, BD Biosciences).

Histology of *in vivo* labeled leukocytes in GL261 tumors

Three 8-week-old female mice were stereotaxically implanted with GL261 tumors. Mice were sacrificed 13 days later. 24 hours and 15 minutes before transcardial perfusion with ice-cold PBS and brain extraction, mice were injected with 200 ug/kg bw CD45-BB515 and CD45-PE, respectively. Whole brains were dissected and embedded in Optimal Cutting Temperature compound (Sigma-Aldrich). The blocks were laid on dry ice to freeze. 10 μm sections were cut using a LEICA CM1950 cryostat. Next, sections were fixed with 4% PFA at room temperature for 10 minutes, then washed with PBS three times, followed by 2 hours blocking (5% FBS, 1% BSA and 0.2% TritonX100) at room temperature. Sections were incubated with APC-conjugated CD31 (MEC13.3, Cat#

102509, 1:100, BioLegend) overnight at 4 °C. DAPI nuclear stain was added for 10 minutes. Sections were mounted with SlowFade (Invitrogen, Cat# S36937) and sealed with coverslips. Imaging was performed using Andor Dragonfly spinning disk confocal microscope. Images were cropped to contain tumor tissue and downscaled by a factor of 0.5 using ImageJ. Segmentation and quantification was done with CellProfiler.[93]

Single cell isolation and sorting for RNA sequencing

Tumor-bearing mice were sacrificed 13 days after tumor inoculation. Mice were deeply anaesthetized by intraperitoneal injection of ketamin 10 mg/ml (Ketavet Veterinary, 100mg/ml, Zoetis) and xylazine 2 mg/ml (Sedaxylan 20mg/ml, Eurovet). Mice were transcardially perfused with 10 ml of ice cold PBS. After brain extraction, tumors were dissected to reduce the amount non-tumorous brain tissue in downstream analyses. Samples were blade-minced on ice and transferred to 1.3 ml digestion buffer (0.0125 mg/ml dNase type I (Roche) and 1 mg/ml collagenase IV (Worthington) in RPMI-1640 (Gibco, 21875-034). Samples were incubated for 20 min at 37 °C, during this incubation samples were mechanically dissociated with syringes (gauge 26). Cells were then transferred to ice and filtered through a 100-μm cell strainer, washed with ice-cold FACS buffer (0.5% BSA, 2 mM EDTA in PBS), and centrifuged (5 min, 4 °C, 350g). Supernatant was aspirated and samples were resuspended in 37% Percoll (Sigma, Cat# GE17089101) density gradient, followed by centrifugation at 800 g, 30 min at 4 °C. The cell pellet was washed PBS, followed by Fc-blocking (1:200) (TruStain FcX, Clone 93, BioLegend) and staining with CD45-APC (30-F11, BD Biosciences). DAPI 0.1 μg/ml (BioLegend) was used for live/dead stain. Cells were filtered through a 70 μm cell strainer. Cell sorting was done on BD FACS Symphony 6 flow cytometer (BD Biosciences). Dead cells and doublets were excluded by gating, after which $CD45^+$ cells were gated based on APC fluorescence, followed by gating for the *in vivo* CD45 stains. Single cells were sorted into 384-well capture plates either by the *ex vivo* CD45-APC stain, or by sorting cells harboring any of the *in vivo* CD45 stains. Capture plates contained 100 nl of lysis solution, 3 μl of mineral oil and 20 nM barcoded poly(T) reverse transcription primers for scRNA-seq. After sorting, plates were first centrifuged and then snap-frozen on dry ice and stored at –80 °C. Cells were analyzed using BD FACSDiva software (BD Bioscience) and FlowJo software (FlowJo LLC).

Colon, lung and blood processing for Zman-seq

Mice (5-weeks-old) were treated with the Zman-seq (n = 3, +1 non-stained control) protocol with timestamping antibody injections 48 (CD45-PE), 36 (CD45-BB515), 24 (CD45-BUV737), 12 (CD45-BV711) hours prior to tissue harvesting. Blood was sampled from the heart, then mice were transcardially perfused with PBS. Blood was washed and incubated with 1 ml 1x ACK lysis buffer (Thermo Fisher, Cat# A1049201) for 5 min at RT. After washing and centrifugation, leukocytes were resuspended in FACS buffer and kept on ice until staining.

Lungs from perfused mice were cut into small pieces and digested for 60 minutes at 37°C with digestion buffer containing collagenase IV (final 0.2 mg/ml) and DNase I (final 0.05 mg/ml) in RPMI-1640 medium supplemented with 10% FBS. Next, tissue pieces were dissociated with syringes. Cell suspensions were passed through a 70 μm strainer, washed and centrifuged. Cells were resuspended in FACS buffer and kept on ice until staining.

Colon was opened longitudinally, cleaned, cut into 0.5 cm long sections and washed with PBS. Colon tissues were incubated in PBS with 5 mM EDTA and 2 mM DTT at 37°C for 20 min to detach epithelial cells. Colon pieces were vigorously shaken up and down for 15 seconds by hand. The remaining tissue was washed with PBS twice to remove EDTA. Next, tissue was then cut into small pieces and was added to the digestion solution and incubated at 37°C for 60 minutes. Digested tissues were dissociated with syringes, passed through a 70 μm strainer, washed and centrifuged. Cells were resuspended in FACS buffer and kept on ice until staining. Leukocytes were stained with CD45-APC stain and DAPI. $CD45\text{-}APC^+$ cells were sorted with BD FACS Symphony 6 sorter into barcoded capture plates for scRNAseq.

Single cell library preparation

The scRNA-seq libraries were created using a revised version of the massively parallel scRNA-seq technique.[89,90] The process involved capturing polyadenylated mRNA from individual cells that had been sorted into 384-well plates, and then barcoding the mRNA during the reverse transcription into cDNA. The resulting cDNA was then pooled for each plate, and underwent fragmentation and amplification to generate sequencing-ready libraries for Illumina sequencing. Quality and DNA concentration tests were performed on each library created from a plate.

Read alignment

The scRNA-seq libraries were pooled at equimolar concentrations and sequenced on an Illumina NovaSeq 6000 sequencer with a sequencing depth ranging from 10k to 50k reads per cell. Reads were condensed into original molecules by counting same unique molecular identifiers (UMI). We ensure that the batches for analysis showed a low level cross single-cell contamination (less than 3%) by statistics on the detected spurious UMI in empty wells. Alignment of reads was done using the MARS-seq2.0 pipeline. In short reads were filtered for low quality reads, subsequently mapped to the mouse reference genome mm10 using HISAT (version 0.1.6), excluding reads with multiple mapping positions.[89] The UCSC genome browser was used as a reference to assign exonic reads to genes. Cell UMI uniqueness was tested for 3kb aria. In cases where exons of different genes shared a genomic position on the same strand, reads were considered as a single gene with a concatenated gene symbol.

Time bin assignment

To assign a tumor exposure time bin to each cell, we classified the fluorescent FACS signal of each time stamp into stained or non-stained (Figure S2A). As the fluorescence signal is variable in each cell due to their diversity in size and cell types as well as autofluorescence, the fluorescence cutoffs could not be generalized. To this end, we additionally sorted CD45+ unstained cells to build our classification model. For each fluorescence time stamp, we trained a second order individual generalized linear model (GLM) with forward scatter (FSC), side scatter (SSC), and DAPI channels as model predictors. Our assumption is that the forward and sideward scatters account for the diverse cell types and ensure that we have an unbiased GLM model across different cell types. Formally, let each fluorescence channel be denoted as Y_i and $x = [x_1, \ldots, x_p]$ be the vector predictor variables (where $p = 7$ for DAPI, three forward scatter channels and sideward scatter channels respectively). We define the generalized linear model of second order interactions with gaussian link as:

$$Y = \sum_{i=1}^{p} \beta_i x_i + \sum_{i=1}^{p} \beta_{ij} x_i x_j + \epsilon$$

where $\epsilon \sim N(0, 1)$ is the independent identically distributed normal error. We check that the residuals of the model are normally distributed by assessing plotting the residuals against the fitted values as well as Q-Q plots. Then cells with measured fluorescent values of $p < 0.001$ were considered as stained. Finally, we assign a tumor exposure time bin to each cell based on the positive antibody stain, which in case of multiple positive stains was determined by the last stain the cell was exposed to in the circulation (Figure S2A).

We also developed an approach for feeding the GLM with unstained FACS events without index sorting. For this, we first manually defined the cutoff for unstained cells in stained samples. Then we applied the same generalized linear model on unstained samples falling into the manually defined cutoff.

MetaCell Construction

We used the R package MetaCell[20] to analyze the single-cell data in the paper. We first removed specific mitochondrial genes, immunoglobulin genes, ribosomal genes, and genes linked with poorly supported transcriptional models (such as those annotated with the suffix "Rik" and so on). We also discarded cells with less than 300 UMIs from the subsequent analysis. Informative genes with high dispersion were selected using the variance-to-mean parameter $T\_vm > 0.1$ and minimum total UMI count > 100. To construct the metacells, we used standard parameters of K = 100 and 750 bootstrap iterations to resample 75% of the cells in each iteration to ensure homogeneity within each metacell. Cells across treatment conditions were combined for metacell construction in the treatment data (Figures 4 and 5) for global characterization. Metacells were then manually annotated based on analysis of marker genes and known cell type markers.

In the initial clustering of the metacells, we identified the major clusters of myeloid and lymphoid cells, as well as doublet contaminations. We then removed the doublet metacells and manually annotated the clustering of the myeloid and lymphoid clusters separately. We combined the clusters if there were no significant difference in their marker genes and annotated them with known cell type markers (e.g. *Clec9a* – cDC1, *C1qa* – TAMs, Arg1 – Arg1 TAM, *Ace* and *Chil3* – Monocytes, *Foxp3* – Treg, *Prf1* and granzymes – NKs, and so on).

The 2D projection of metacells is computed using a force-directed layout algorithm on the regularized similarity metacell graph GM as described in the MetaCell algorithm.[20] For the single cell projection, first we compute a raw similarity matrix using Pearson's correlation and then construct a weighted adjacency matrix to define a directed cell graph G. Cells are then positioned by taking the average metacell coordinates of filtered neighbor cells from G.

MetaCell Time Trajectory Construction

To estimate a continuous tumor exposure time (cTET) profile for each metacell, we used the distribution of each time point within each metacell to calculate the corresponding cumulative distribution (CDF) and area under curve which we define as cTET (top panel of Figure S3B). Specifically, let us denote a distribution of timepoints TP_i where $i \in \{0, 12, 24, 36, 48\}$ time bins. For each metacell, the CDF of $P(X \leq i)$ is defined as the normalized proportion of each time point TP_i. Then we estimate the cTET values as $cTET = 1 - \frac{AUC - \min(AUC)}{\max(AUC) - \min(AUC)}$ using the area under curve (AUC) of the CDF. Since earlier time bins correspond to a larger AUC, we renormalize the cTET such that $cTET \in [0, 1]$ and that smaller cTET indicates an earlier time bin.

We then refine the cTET profile to construct the trajectory of cell differentiation along tumor exposure time (bottom panel of Figure S3B). First, we construct a base reference trajectory $T_r = [t_1, \ldots, t_n]$ where $t_i \in [0, 1]$ that shows the transitioning of cTET by taking the average cTET in each of the annotated cell type cluster. The trajectory is ordered by the average cTET and we plot the arrows according to the cTET values. Subsequently, we performed a correlation-based unsupervised clustering on the top informative cell type specific genes for $k \in [3 \ldots N]$ as described previously.[94] Briefly, we used the dispersion ratio to select the top informative genes and performed a hierarchical clustering on the normalized Spearman correlation distance matrix to obtain unbiased cell type clusters. Then for each k, we construct a clustering trajectory T_k by ordering the cluster average cTET. We define the refined cTET profile by the combined trajectory as follows:

$$T_c = \alpha . T_r + \beta . \frac{\sum T_k}{(N - k)} \text{ where } \alpha = \beta = \frac{1}{2}$$

Temporally-resolved Trajectory Analysis

We utilized the refined cTET trajectory to delve deeper into the molecular changes across time in the transitioning of cell types (e.g. chemotactic NKs to dysfunctional NKs). We used the Spearman's rank correlation to first identify top genes which are significantly correlated with cTET ($p < 0.05$). The expression of the top genes were then smoothed across cTET using loess fitting and each gene was re-normalized to [0, 1] across all metacells. Groups of up-regulated, down-regulated, and transiently-regulated gene modules were then visualized as heatmaps by clustering genes of similar patterns together.

To further investigate the underlying mechanisms that drive the gene regulations, we infer the TF activity of each metacell, followed by the same correlation analysis and loess smoothing across cTET as mentioned above. The TF activity was estimated using the Dorothea[31] database with genes of confidence levels of "A" and "B". The top correlated TF activities are shown as heatmaps showing the shift of TF regulation across time.

Projection of publicly available NK cell signatures

To investigate the emergence of NK cell subtypes across time in the context of the literature, gene signatures reported in Ducimetière et al.[22] have been retrieved and filtered for average $\log_2$(fold change) expression > 0. The obtained gene signatures have been scored in MCs of the NK cell compartment by computing the average expression across gene signatures in MCs and subtracting the aggregated expression of 100 control feature sets using Seurat's AddModuleScore implementation.[95,96] Expression scores for each gene signature per MC have been smoothed using a polynomial fit and visualized in lineplots using ggplot2.

Differential gene analysis

We used a pseudo-bulk approach to identify differential genes between the *Acp5* TAMs (enriched in the aTREM2 antibody treatment) and *Arg1* TAMs (enriched in the control antibody treatment). The gene counts were first summed within each individual mouse as pseudo-bulk samples, resulting in 3 aTREM2 treated samples and 3 control-treated samples. Then DESeq2[97] was applied to normalize the counts and to perform differential gene analysis. The top genes were visualized in Figure 5D as volcano plot with a threshold of p-value < 0.001 and $\log_2$ fold change > 0.5.

Ligand receptor analysis across time

To estimate ligands in the TME that may drive the observed changes in gene expression upon entering the tissue, Nichenet was utilized.[98] Genes which showed significant correlation with cTET across metacells were considered as target genes in the receiver population (e.g. NK cells or monocytes). Background genes were defined as genes expressed in (at least 5% of the cells in) the receiver population and did not show significant correlation with time. Potential ligand-receptor pairs, controlling the observed time-dependent changes in target gene expression, were restricted by receptors that are expressed in the receiver cell population. Ligands were not restricted to be expressed by putative sender cells within the dataset in order to assess TME ligands being produced by non-immune cells such as tumor cells or the stromal compartment. Ligands were prioritized based on the binary Pearson's correlation of whether a gene significantly correlates with time and their respective ligand-target regulatory potential. Ligand-target regulatory potential indicates how strong a ligand is associated with a given target gene based on prior knowledge and is presented in Nichnets integrated weighted networks. To estimate the cumulative downstream activity of a predicted ligand, the weighted average expression of downstream genes for the specific ligand was computed. For this, the gene expression of each target gene in the subset has been scaled between 0 and 1 and weights for the weighted average have been retrieved by the respective regulatory potential of each ligand-target gene pair. For target genes for which a negative correlation with time was observed (Pearson correlation coefficient $r < 0$), the weighted expression was multiplied by -1.

Analysis of scRNAseq data of *in-vitro* differentiated BMDMs

ScRNAseq data of BMDMs have been pre-processed using the MetaCell package as described above. Downstream analysis has been performed in python 3.9. QC-filtered raw counts have been processed using the scanpy framework,[99] normalized, log1p transformed and the top 2000 highly variable genes have been retrieved. To resolve the effect of experimental covariates such as concentration of GBM supernatant in cell culture medium or antibody treatment (aTREM2, control antibody or PBS control) on the single cell profiles, probabilistic modeling using MrVI has been employed.[100] The model has been trained using the raw counts of the 2000 most variable genes. The sample-infused latent representation z has been used to compute the neighbor graph and UMAP representation using scanpy. The sample-sample distance matrix has been computed in MrVI without prior classification into cell types. Dot plots of selected genes have been generated in scanpy.

Interaction analysis upon TREM2 inhibition

To investigate the effect of TREM2 inhibition with antagonistic aTREM2 antibody on remodeling the TME in GL261-bearing mice, first, the Trem2-expressing and -responding cells were determined. Dotplots displaying Trem2 expression across cell subsets were generated using Seurat v4.3.0.[96] To estimate cell types altered upon TREM2 inhibition, differential gene expression between cells of aTREM2-treated mice and control-treated mice were computed for each cell type using a Wilcoxon Rank Sum test with Bonferroni correction for multiple testing. To investigate downstream effects upon TREM2 inhibition and identify putative ligands mediating the

reorganization of the TME, Nichenet has been employed.[98] For this, Trem2-expressing cells (TAMs and monocyte-derived macrophages) were defined as sender cells (since these were affected by the aTREM2 treatment) and potential ligands have been extracted that are expressed in at least 5% of cells within either of the two clusters. Potential ligands have been further restricted by filtering ligand-receptor pairs in which the cognate receptor is expressed in at least 5% of the receiver cell population.

To investigate autocrine signaling networks in response to TREM2 inhibition, ligands expressed by Trem2-expressing cell types have been prioritized based on their ability to predict the observed changes in target gene expression in TAMs. To provide further evidence that identified ligands may mediate the observed changes in target gene expression, ligands have been filtered to show an absolute average $\log_2$(fold change) of > 1 in response to TREM2 inhibition. Thus, ligands are prioritized by both their ability to explain changes in target gene expression based on reported ligand-target interactions in receiver cells, and their differential abundance in sender cells.

To investigate indirect paracrine effects of TREM2 inhibition in leukocytes within the TME, Trem2-expressing cells have been defined as sender cells and cell types lacking Trem2 expression but changing in response to aTREM2 treatment as potential receiver cell types. To assess to what extent the identified set of signaling ligands may explain changes in downstream target gene expression of neighboring leukocytes in the TME, hypergeometric tests have been performed using the stats package. For this, the overlap of target genes regulated by the set of signaling ligands (99th percentile regulatory potential for each ligand) has been compared to the differentially expressed genes upon TREM2 inhibition in the respective cell population.

Circos visualizations have been drawn using the circlize package. All other visualizations have been drawn using ggplot2.

Projection of Zman-seq derived gene signatures on human GBM

For clinical and human relevance, we wanted to assess how the Zman-seq derived genes can be utilized in human GBM. We analyzed published data from newly diagnosed GBM patients focusing on myeloid cells.[24] Using the code provided by Pombo-Antunes and colleagues on github, we recapitulated their analysis in Seurat and produced the 2D UMAP projection plot with their provided annotations (Figure S5E-left) and showed top relevant genes from our gene set. We used the mouse-human orthologs to convert mouse genes to human genes, and used the AUCell[101] package to score the set of genes for each single cell in the human data. Based on the annotations, we then calculated the average score for each cell type annotation and re-normalized the scores to 0 to 1 for visualization (Figure S5E-right).

Survival analysis of human GBM patients

To assess whether expression of a given ligand is significantly associated with overall survival in human GBM patients, GEPIA (Gene Expression Profiling Interactive Analysis) has been utilized based on the The Cancer Genome Atlas Program (TCGA).[87] GBM patients have been stratified based on the 75th percentile of CCL5 expression and the hazard ratio of CCL5 expression for overall survival has been tested using a Mantel-Cox test.

RNA velocity and pseudotime benchmarking with Zman-seq

To benchmark how velocity inference performs on our empirical dataset and depict the variation between different gene selection methods, we applied scVelo[102] on single cell RNA seq data of monocytes and macrophages of mice treated with an anti-TREM2 blocking antibody and isotype control (Figure S6). We applied the dynamic model from scVelo using 2000 highly variable genes (Figure S6A), and observed reverse differentiation directions from MonMac1 to monocytes. We hypothesized that this is highly dependent on the number and selection of genes which had sufficient spliced / unspliced transcripts to be fitted with the velocity model. For instance, we show in Figure S6B that the velocity is nicely fitted for *Arg1* and *Hif1a* but not for *Cd274* and *Il18bp* despite the observed gene expression pattern. The performance of velocity inference is highly dependent on the selected genes as well as genes which could be fitted by the rate of spliced and unspliced transcripts. In order to quantify the results, we pooled the single cells and calculated the averaged inferred latent time per metacell to compare with our AUC time (Figures S6C and S6D). Although our Zman-seq derived genes increased the correlation, we can observe in Figure S6D (panel 1) that the latent time mainly improves accuracy of differentiation estimation in the TAMs (Cd72_TAMs and Arg1_TAMs), bringing them closer to the empirically determined AUC. We calculated a deviation distance metric to show the total Euclidean distance that the inferred latent time deviates from the AUC, and the results are concordant with the spearman correlations.

Similarly to RNA velocity inference, we benchmarked pseudotime algorithms on our empirical single-cell dataset. Since pseudotime algorithms can be applied on gene expression matrix independent of spliced and unspliced transcripts, we tested various algorithms including DPT, Palantir, Monocle2, redPATH, and SCORPIUS[5,94,103–107] on the metacells. We downsampled the number of UMIs on the aggregated metacell gene expression matrix before normalization to ensure that each metacell is comparable to a single cell. We used the top 1000 HVGs, gene ontology (GO) selected genes as previously described,[94] and Zman-seq derived genes for comparison (Figure S6E). It is worth mentioning that both DPT and Palantir are semi-supervised requiring a prior defined starting node which we assigned based on the earliest AUC, whereas the other algorithms were run fully unsupervised. Both Zman-seq derived genes and GO selected genes greatly increased the correlation performance and the deviation distance metric showed a similar pattern (Figures S6F–S6J). Although the correlation values were similar for redPATH, DPT, and Palantir, we showed that each algorithm performed quite differently in Figure S6H-J respectively. redPATH showed concordant results in the TAMs but the pseudotime was earlier in the MonMac2 population; DPT showed similar performance in the TAMs, but assigned later pseudotime

for monocytes, MonMac1 and MonMac2; and lastly Palantir was affected by a few outliers in MonMac1 and MonMac2 populations. Taken together, we showed that current pseudotime algorithms are similarly highly dependent on gene selection. We propose that for cell type specific differentiation, using prior knowledge genes such as Gene Ontology genes[94] vastly improve the pseudotime reconstructions.

QUANTIFICATION AND STATISTICAL ANALYSIS

Plots and analyses were generated with R and are detailed in the respective methods sections including the statistical tests used. Statistical details such as error estimation and number of replicates are provided in the respective figure legends.

Microscopy images were analyzed with open-source ImageJ and CellProfiler.

CellPress

Supplemental figures

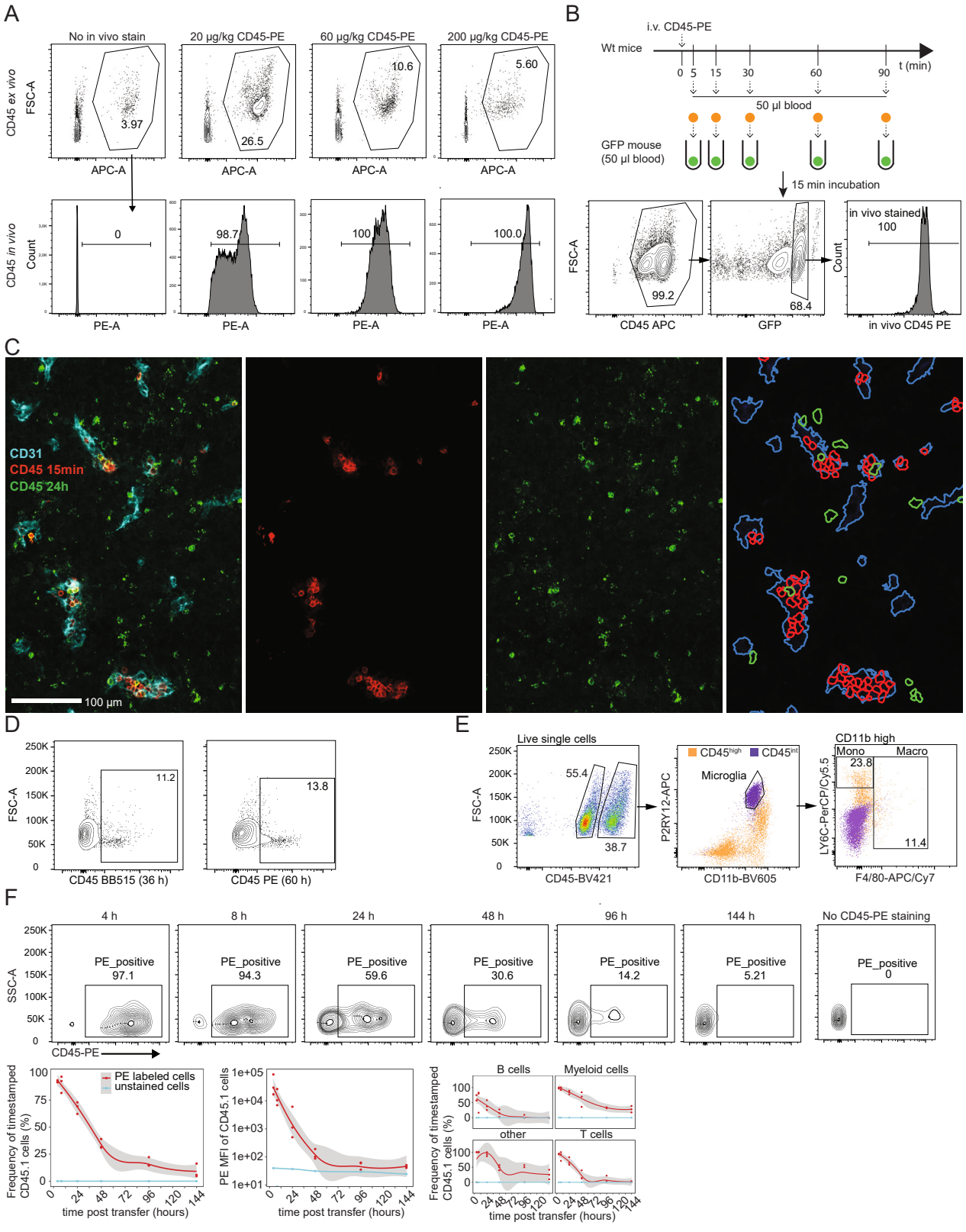

(legend on next page)

Figure S1. Zman-seq facilitates tracing of transcriptomic cell states *in vivo* across time, related to Figure 1

(A) Flow cytometry density plots and histograms of $CD45^+$ PBMC after increasing concentrations of CD45-PE antibody intravenous injections. Error bars indicate mean and 90% CI (n = 3).

(B) Schematic illustration of the measurement of unbound CD45 antibody in the blood. Three wild-type (WT) mice were injected with CD-45-PE antibody and blood was drawn after 5–90 min. Each sample was mixed with equal amounts of blood from a ubiquitously GFP-expressing mouse. Percentage of PE^+ GFP^+ cells were determined with FACS.

(C) Fluorescent images of a GL261 brain tumor after mice were i.v. injected with CD45-PE and CD45-BB515 antibodies 15 min and 24 h before brain extraction, respectively. Samples were prepared for microscopy and were stained for endothelia with CD31-APC antibodies. Endothelia, 24 h and 15 min labeled cells were segmented and for quantification (see also Figure 1D).

(D) Flow cytometry density plots of $CD45^+$ cells from GL261 tumor after intravenous fluorescent CD45 antibody injections 36 and 60 h (see also Figure 1E) before tumor extraction.

(E) Flow cytometry dot plots of $CD45^+$ cells from GL261 tumor showing the distinction between microglia ($CD45^{int}$, $CD11b^{high}$, $P2RY12^{high}$, $F4/80^{low}$, $LY6C^{low}$), and monocytes ($CD45^{high}$, $CD11b^{high}$, $P2RY12^{int}$, $F4/80^{low}$, $LY6C^{high}$) and macrophages ($CD45^{high}$, $CD11b^{high}$, $P2RY12^{int}$, $F4/80^{high}$, $LY6C^{low}$).

(F) Flow cytometry density plots of CD45-PE antibody-stained $CD45.1^+$ positive cells in the blood, 4–144 h after intravenous injection of CD45.1 cells into CD45.2 mice (n = 3, +1 control receiving CD45.1 PBMC without CD45-PE antibody stain) (upper lane). Each density plot (4–144 h) is generated from the pooled events of 3 mice. Regression plots (lower lane) of CD45-PE antibody-stained CD45.1 cells from total CD45.1 cells over time. Regression plot of median fluorescent intensity (MFI) of CD45-PE antibody-stained CD45.1 cells over time. Gray shading represents 95% confidence interval.

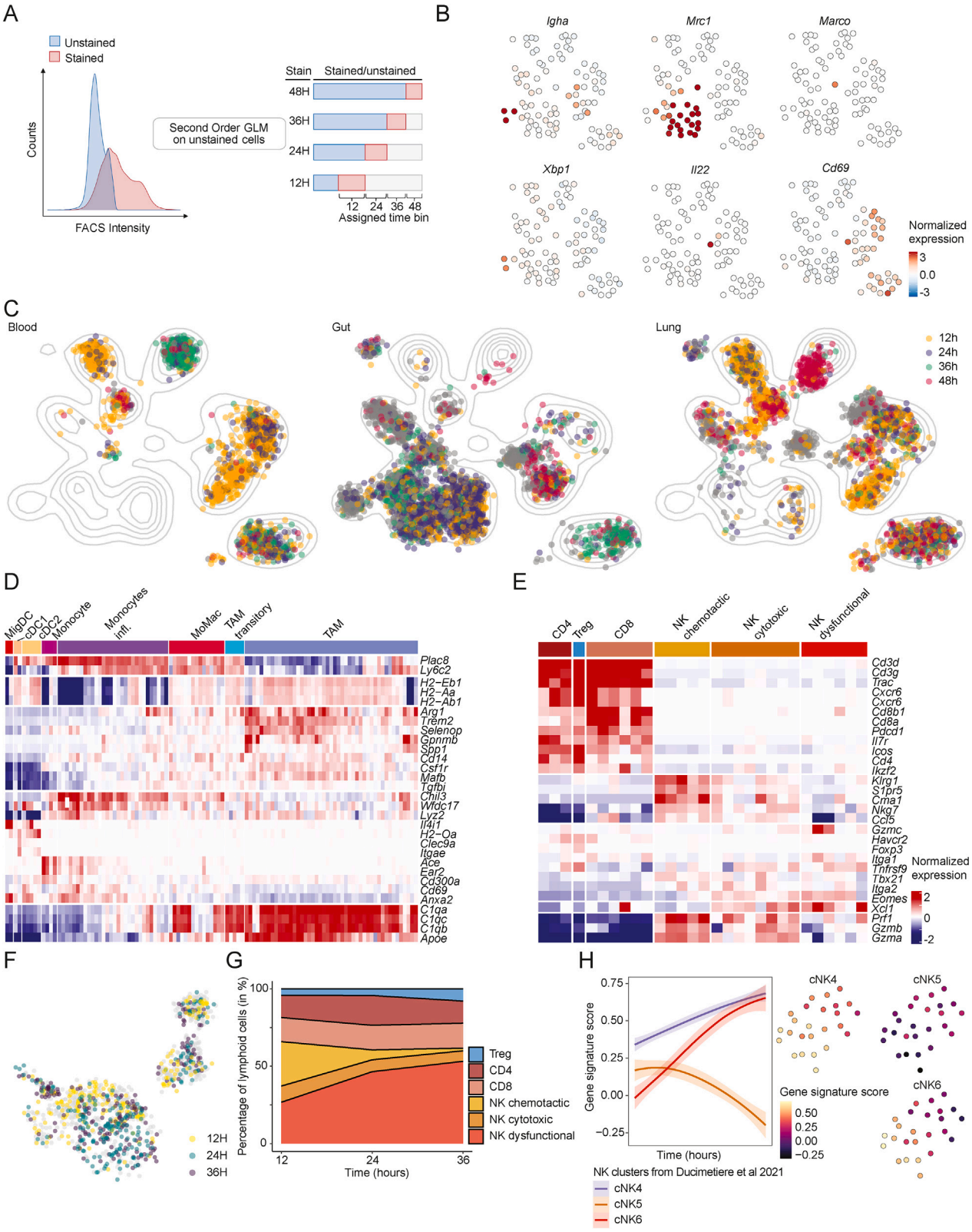

(legend on next page)

Figure S2. Zman-seq in blood, colon and lung in steady state, and dynamic gene expression profile of murine leukocytes in the tumor, related to Figures 1 and 2

(A) Schematic illustration of time bin assignment. The left panel shows the distribution of stained and unstained cells with FACS intensity (one for each time bin) on the x axis and the frequency count on the y axis. We apply a second-order GLM model on the unstained cells to determine the threshold for stained cells for each time bin. The right panel depicts the approach to assigning the time bin after classifying the stained cells. The stained cells are assigned to the "latest" time bin that they were exposed to.

(B) Marker gene projections of $\log_2$ normalized footprint expression on $CD45^+$ cells from colon, lung, and blood after 12-, 24-, 36-, and 48-h Zman-seq time stamps.

(C) Single cells colored by time bin and projected on the metacell graph. The plotted points indicate all cells from the specific organ, respectively, and the contours indicate the density of all cells from three organs on the metacell graph, see also Figure 1G.

(D) Heatmap showing the top markers for defining the major myeloid clusters. The expression is defined as the $\log_2$ footprint (expression over the median) and normalized within the myeloid cells only.

(E) Heatmap showing the top markers for defining the major lymphoid clusters and is normalized in the same approach as described in (A).

(F) Single cells from each labeled time bin downsampled to 200 cells per time bin from $CD45^+$ gated cells (see also Figure 2C).

(G) Stacked percentage area plot that shows the relative percentage of lymphoid cells at each time bin (12, 24, and 36 h, respectively). The color depicts the different annotated cell-type clusters.

(H) Line plots (top) showing the weighted expression of published gene signatures in NK cells across time. Weighted expression has been smoothed using a polynomial regression model and mean and 90% confidence intervals (shaded area) are shown. MC maps of NK cells (bottom) are colored by the weighted gene signature scores.

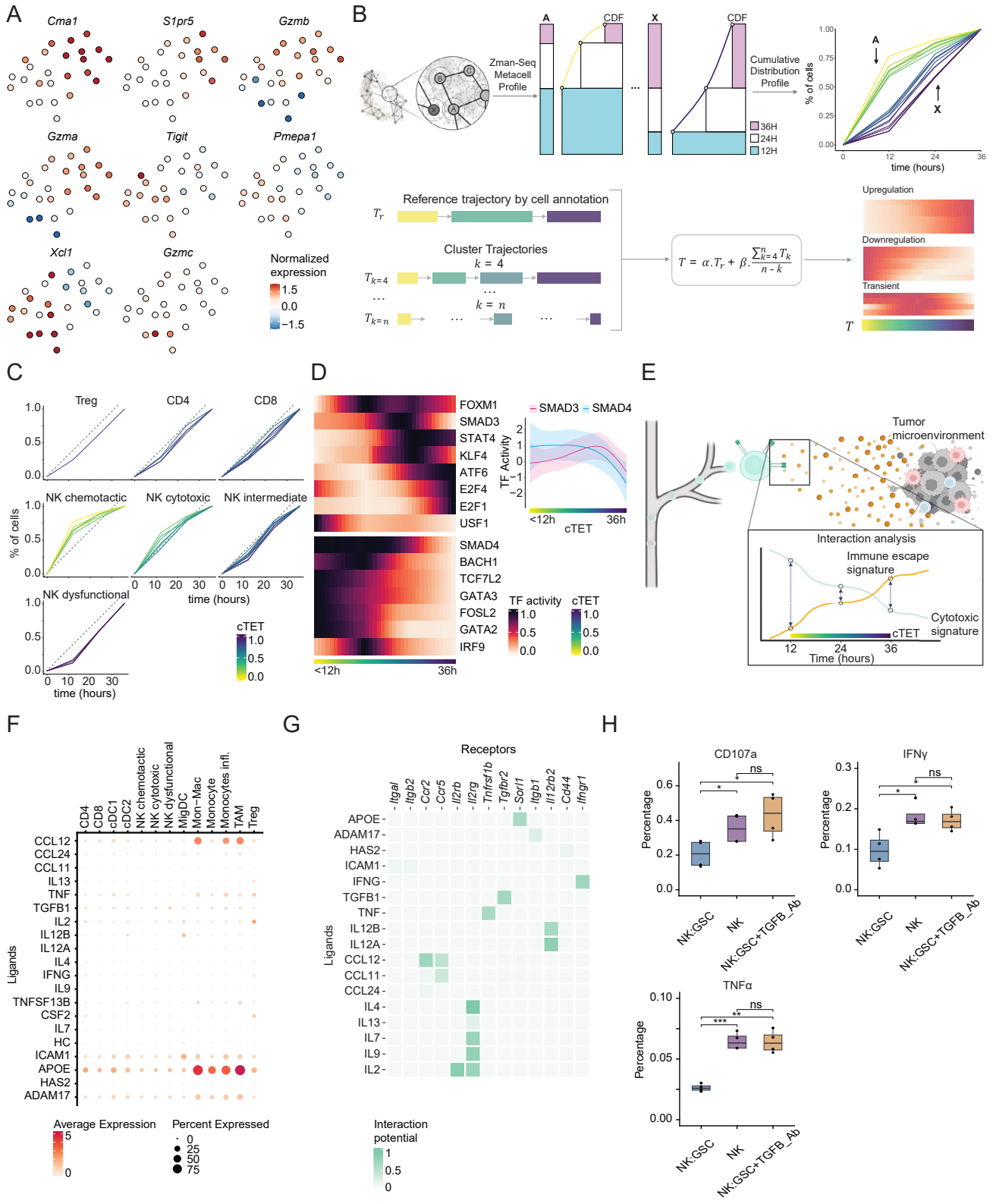

(legend on next page)

Figure S3. Zman-seq reveals temporal NK cell trajectories in the tumor, related to Figure 3

(A) Marker gene projections of log_2 normalized footprint expression on NK cells only, showing the transitioning from chemotactic NK to dysfunctional NK.

(B) Schematic analytical workflow and methods developed for Zman-seq. The top panel illustrates the approach to define cTET using the cumulative distribution (CDF) profile for each metacell. The bottom panel depicts the construction of temporally resolved trajectory across time and identification of significant marker genes across time.

(C) The CDF profile for each cell type is plotted separately, with the mean CDF plotted as a dotted line across the center. Each line depicts a metacell and is colored by the cTET.

(D) Heatmaps of significant TF activity along cTET in the NK metacells only. Each row is normalized and smoothed according to the cTET of each metacell and shows the transitioning of TF activity from chemotactic NK to dysfunctional NK as ordered by cTET. Line plots (right) show the normalized TF activity in the NKs across time for SMAD2 and SMAD3. The TF activity has been smoothed using a polynomial regression model, and the 95% confidence interval is shown as the shaded area.

(E) Schematic representation of applied interaction analysis. Ligands acting on leukocytes in the TME are predicted by correlating time-dependent target genes in leukocytes with documented ligand-target gene databases.

(F) Dot plot displaying the gene expression of prioritized ligands that best explain temporal changes in target gene expression in NK cells (as presented in Figures 3F and 3G). Dot size indicates percentage of cells expressing the respective gene, and color indicates mean normalized gene expression for each cluster.

(G) Heatmap showing the interaction potential between prioritized ligands and their cognate receptor in NK cells.

(H) The effect of TGFβ-blocking antibody on the expression of TNF-α and IFN-γ, and the degranulation (CD107a) of human NK cells co-cultured with human glioma stem cells. Each dot represents a sample and the box extends to the 25^{th} and 75^{th} percentile with median in bold line.

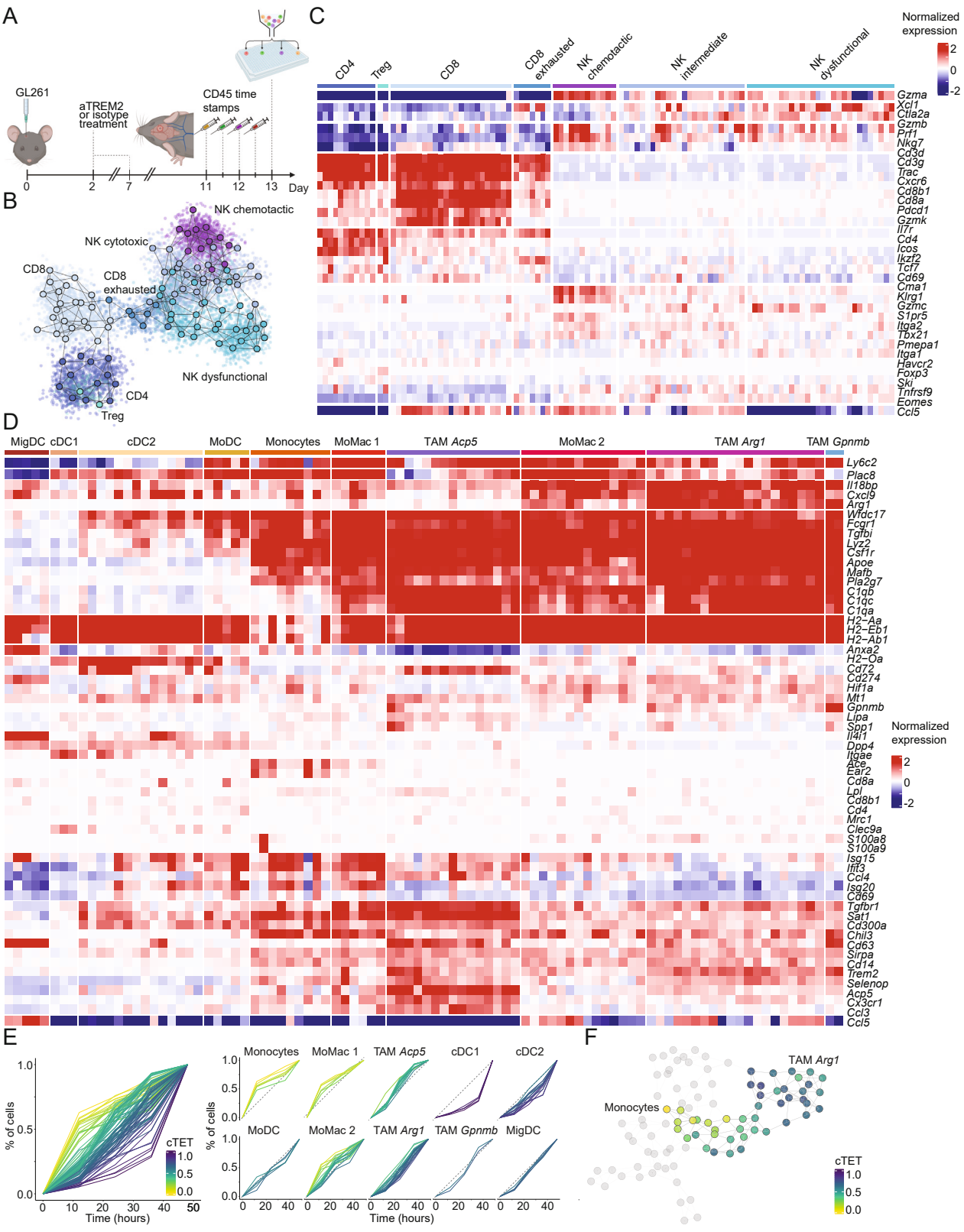

(legend on next page)

Figure S4. Dynamic gene expression profile of leukocytes in brain tumors upon aTREM2 immunotherapy, related to Figure 4

(A) Schematic illustration of investigating aTREM2 immunotherapy with Zman-seq.

(B) Metacell graph projection of lymphoid cells consisting of 107 MCs representing 7,857 single cells sorted from 3 control antibody-treated mice and 3 aTREM2-treated mice on $CD45^+$ gating.

(C and D) Heatmap showing the top markers for defining the major lymphoid (C) and myeloid (D) clusters. The expression is defined as the log_2 footprint (expression over the median) and normalized within the lympohid cells and myeloid cells separately.

(E) CDF profile line plot for the myeloid cells only. The metacells are shown in each individual cell-type cluster on the right, and the diagonal dotted line represents the mean CDF as a reference line. Each line represents a metacell, and the color depicts the cTET value of the metacell.

(F) Projection of cTET profile on the metacell graph for the monocytes to *Arg1* TAMs only. The other myeloid cell types are shown in gray on the map.

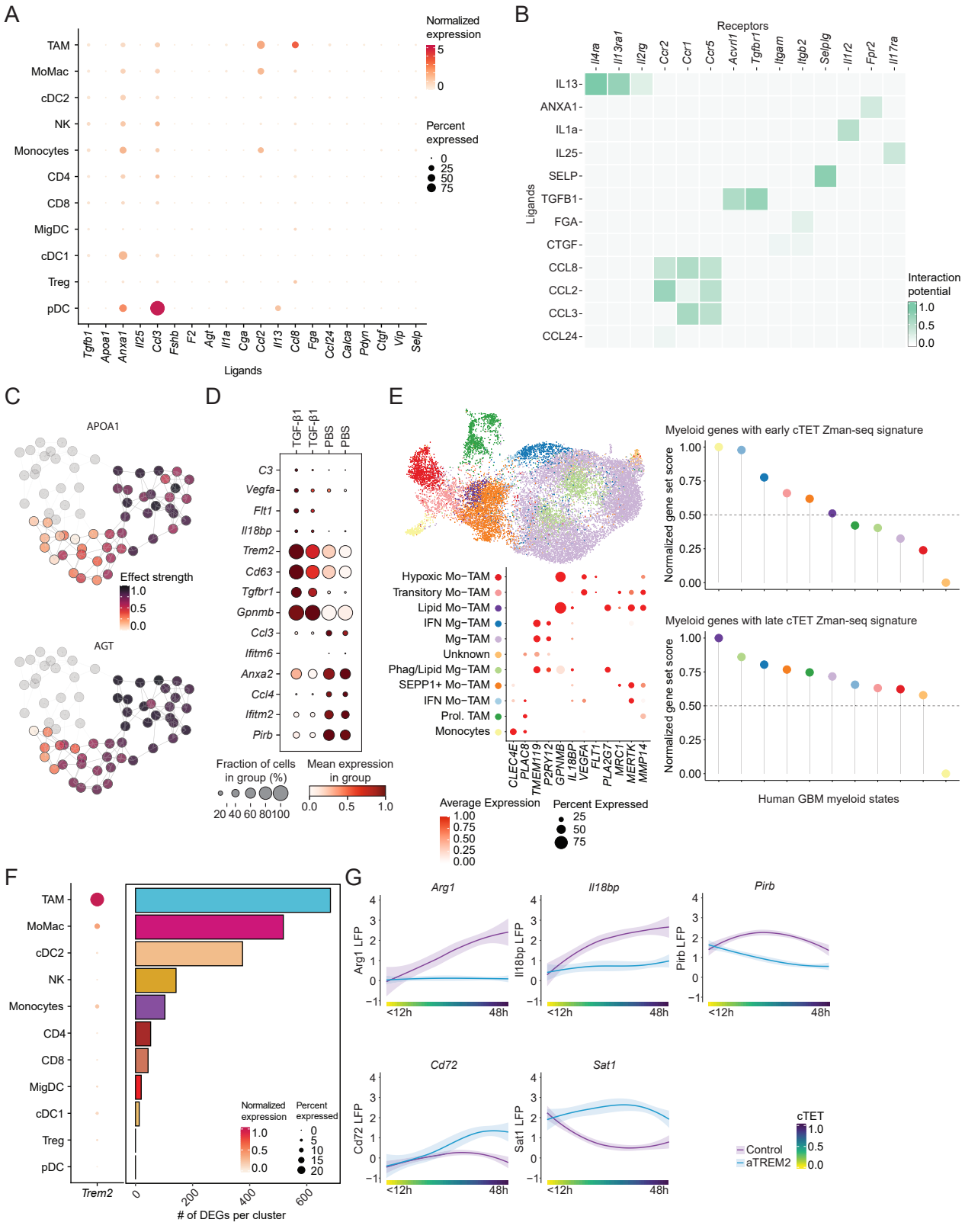

(legend on next page)

Figure S5. Ligand-receptor interactions and metabolic activity of TAMs in brain tumors, and the effect of TREM2 antagonistic antibody on the monocyte-to-TAM transition, related to Figures 4 and 5

(A) Dot plot displaying the gene expression of prioritized ligands that best explain temporal changes in target gene expression in monocyte-derived phagocytes (monocytes, MoMac, and TAMs; as presented in Figures 3F and 3G). Dot size indicates percentage of cells expressing the respective gene, and color indicates mean normalized gene expression for each cluster.

(B) Heatmap showing the interaction potential between prioritized ligands and their cognate receptors in monocyte-derived phagocytes.

(C) MC map displaying the predicted time-dependent interaction between monocyte-derived phagocytes (monocytes, MoMacs, and TAMs) and the TME. MC maps are colored by the scaled weighted cumulative target gene expression, termed "effect strength", of APOA1- and AGT-regulated target genes in monocyte-derived phagocytes.

(D) Dot plot displaying the gene expression of BMDMs after TGF-β1 treatment *in vitro*. Dot size indicates percentage of cells expressing the respective gene, and color indicates mean normalized gene expression for each condition.

(E) Upper left panel shows the two-dimensional UMAP projection of 18,157 integrated myeloid cells from 7 newly diagnosed glioblastoma (GBM) patients and the expression of Zman-seq-derived time-dependent genes (bottom left). The right panel shows the normalized average score of our Zman-seq-derived time-correlated genes on each cell type from the human dataset. Early myeloid genes are genes that significantly correlate with cells harboring early cTET (right top), whereas late genes correlate with late cTET (right bottom). Mo, monocytes; Mg, microglia.

(F) Dot plot (left) displaying the expression of *Trem2* across cell types. Dot size indicates percentage of cells expressing the respective gene, and color indicates mean normalized gene expression for each cluster. Bar graph (right) showing the number of differentially expressed genes in response to aTREM2 treatment for each cell type, determined by a Wilcoxon rank-sum test and Bonferroni correction.

(G) Line plots (right) show the normalized $\log_2$ footprint expression of marker genes in the myeloid cells across time for IgG control (in purple) and aTREM2 treatment (in blue). The normalized expression has been smoothed using a polynomial regression model, and the 95% confidence interval is shown as the shaded area.

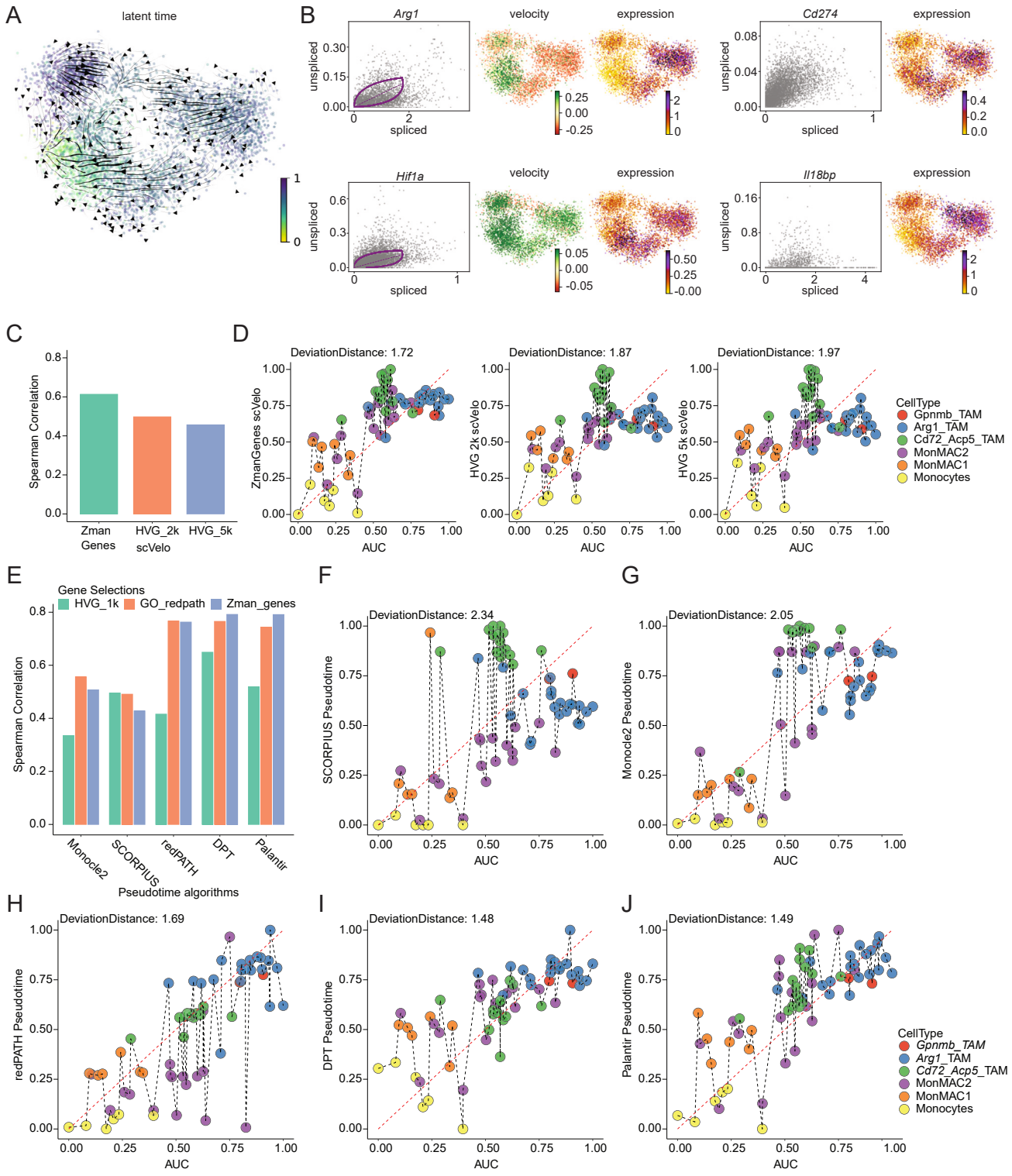

Figure S6. Benchmark with scVelo velocity inference and pseudotime algorithms, related to STAR Methods

(A) Velocities derived from the dynamic model on only monocytes and macrophages at single-cell level, and visualized on the same 2D embedding as shown in Figure 4A. The depicted latent time is inferred from using 2,000 HVGs.

(B) Putative driver genes identified by the dynamic model where Arg1 and Hif1a depict high likelihoods of dynamic behavior and CD274 and Il18bp showed low likelihoods.

(legend continued on next page)

(C) Spearman correlation bar plot showing the correlation between scVelo-derived pseudotime and our AUC by different gene selection methods (Zman-seq-derived genes, 2,000 and 5,000 HVGs, respectively).
(D) Scatterplot showing the relationship between the scVelo-derived pseudotime (y axis) and our AUC (x axis), colored by the annotated cell types on metacells. The shown results are based on Zman-seq-derived genes.
(E) Spearman correlation bar plot showing the correlation between algorithm-derived pseudotime and our AUC with different gene selection methods (top 1,000 HVGs, gene ontology genes with dispersion filter from redPATH, and Zman-seq-derived genes).
(F–J) Scatterplot showing the relationship between the algorithm-derived pseudotime (y axis) and our AUC (x axis), colored by the annotated cell types on metacells. The shown results are based on Zman-seq-derived genes.
The black dotted line shows the AUC order, and red dotted line shows the perfect AUC. The deviation distance shows the Euclidean distance of the inferred pseudotime from the AUC. HVG, highly variable genes.

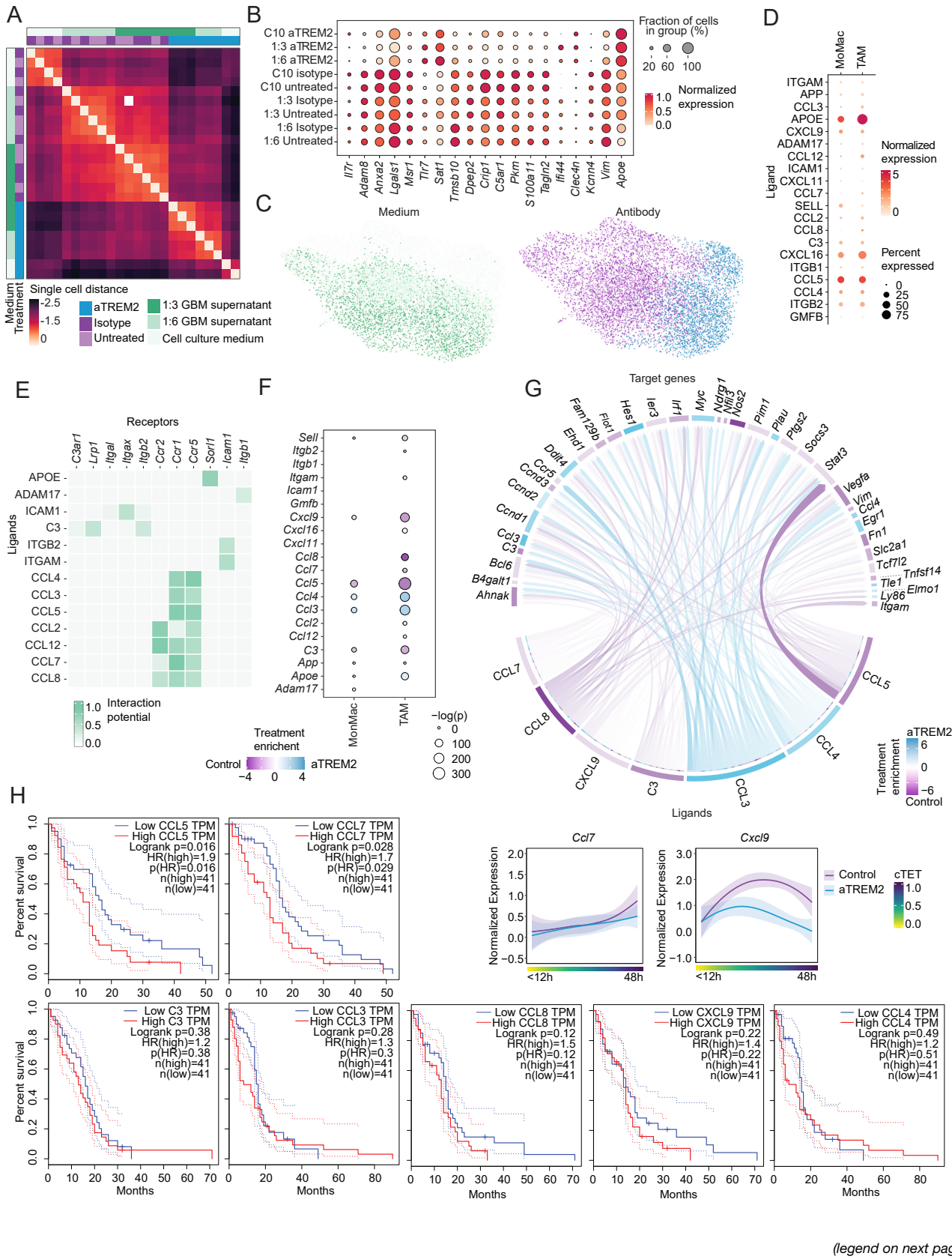

(legend on next page)

Figure S7. TREM2 inhibition of *in vitro* differentiated BMDMs resembles the *in vivo* effect of aTREM2 treatment and reprograms the ligand-receptor interactions in TME *in vivo*, related to Figure 5

(A) Heatmap showing the aggregated single-cell distance matrix of *in vitro* differentiated BMDMs in the presence of TREM2-blocking antibody, isotype, or PBS control. Supernatant of GL261 cells has been used to condition the cell culture medium at different concentrations. Each row/column corresponds to a biological replicate.

(B) Dot plot displaying the gene expression of *in vitro* differentiated BMDMs. Dot size indicates percentage of cells expressing the respective gene, and color indicates mean scaled gene expression for each condition.

(C) UMAP of MrVIs latent space z displaying the effect of GL261-conditioned cell culture medium (left) and aTREM2 antibody or control (right) on *in vitro* differentiated BMDMs.

(D) Dot plot displaying the gene expression of prioritized ligands expressed by *Trem2*-expressing cells that best explain changes in target gene expression in TAMs in response to aTREM2 treatment (as presented in Figure 5A). Dot size indicates percentage of cells expressing the respective gene, and color indicates mean normalized gene expression for each cluster.

(E) Heatmap showing the interaction potential between prioritized ligands and their cognate receptors in TAMs.

(F) Dot plot indicating the differential expression of prioritized ligands between aTREM2-treated and isotype-treated mice, determined by a Wilcoxon rank-sum test and applying a Bonferroni correction. Dot size indicates significance, and color represents average $\log_2$ fold change for aTREM2-treated mice (high = purple, low = blue).

(G) Circos plot indicates the autocrine interaction in TAMs induced by ligands that are produced by *Trem2*-expressing cells (senders) and shows an absolute average $\log_2$ fold chain of more than 1 in response to TREM2 inhibition (as presented in Figure S7F). Color indicates the $\log_2$ fold change enrichment for each ligand upon TREM2 inhibition, determined by pseudobulk analysis using DEseq2 (as shown in Figure 5A). Expression has been smoothed using a polynomial regression model, and mean and 95% confidence intervals (shaded area) are shown.

(H) TCGA analysis showing the survival curves for GBM patients stratified by C3, CCL4, CCL3, CCL5, CCL7, CCL8, and CXCL9 gene expression (high > 75th percentile). Hazard ratio of gene expression for overall survival has been tested using a Mantel-Cox test.

BMDMs, bone-marrow derived macrophages; C10, cell culture medium only.